First Ce-Nd isotope measurements of middle and lower continental crust samples support massive lower crust recycling over Earth's history

Claudine Israel, Maud Boyet, Régis Doucelance, Pierre Bonnand, B. Dhuime, D. Ionov, H. Moreira, M.G. Jackson, A.V. Golovin

First Ce-Nd isotope measurements of middle and lower continental crust samples support massive lower crust recycling over Earth's history

C. Israel[1,2,*], M. Boyet[1], R. Doucelance[1], P. Bonnand[1,3], B. Dhuime[4], D. Ionov[4], H. Moreira[4], M.G. Jackson[5], A.V. Golovin[6]

[1] Université Clermont Auvergne, CNRS, IRD, OPGC, Laboratoire Magmas et Volcans, F-63000 Clermont-Ferrand, France

[2] Université Paris Cité, Institut de physique du globe de Paris, CNRS, F-75005 Paris, France

[3] Univ Brest, CNRS, Laboratoire Geo-Ocean, UMR6538, IUEM, 29280, Plouzane, France

[4] Géosciences Montpellier, Montpellier University, France

[5] Department of Earth Science, University of California, Santa Barbara, CA, 93106-9630, USA

[6] V.S. Sobolev Institute of Geology and Mineralogy Siberian Branch Russian Academy of Sciences, Novosibirsk 630090, Russia

*Corresponding author.

E-mail address: israel@ipgp.fr (Claudine Israel).

ABSTRACT

Long-lived radioactive isotopes provide valuable information on the evolution of Earth's geological reservoirs. Coupled measurements of the ^{138}La-^{138}Ce and ^{147}Sm-^{143}Nd systems have attracted much interest, but some critical reservoirs, such as the deep continental crust, have yet to be investigated. To address this gap, we report Ce-Nd isotope measurements of 35 crustal samples from Canada, western Europe, and Siberia, with Archean to Phanerozoic ages. Most samples from western Europe and Siberia are interpreted to represent the deepest continental crust because of low SiO_2 content (<55 wt.%) and generally mafic compositions. In contrast, Precambrian composites from the Canadian shield have highly felsic compositions (61–71 wt.% SiO_2) and represent the old upper continental crust. Xenoliths from the Massif Central (France) and samples from uplifted massifs in the Ivrea-Verbano zone (Italy) plot on the Ce-Nd mantle array. Precambrian Canadian composites and xenoliths from Udachnaya (Siberian Craton) plot to the left of the mantle array, with the Siberian samples farthest from the array. The La-Ce system yields a ca. 1.8 Ga age for the Siberian xenoliths, distinct from the ca. 2.7 Ga Sm-Nd errorchron age. The La-Ce system was most likely reset during a large-scale episode of delamination and rejuvenation of the Archean lower lithosphere established in Siberia. A change in the La/Ce ratio during this event explains an increasing deviation with time of the Ce-Nd isotopic composition of the Siberian deep crust from the mantle array. We introduce a new parameter (θ) to quantify the likelihood of any rock evolving away from the mantle array. It represents the angle between the evolution vector of a sample and the mantle array, and it is calculated from measured La/Ce and Sm/Nd ratios. Samples that plot to the right of the mantle array have $\theta > 0$, whereas samples that plot to the left of the mantle array have $\theta < 0$. The angle θ was used to compare our samples to a worldwide

granulite compilation (1581 samples) because it is independent of the age and the initial isotopic composition of the samples. The majority of lower crust rocks have negative θ, suggesting they are prone to evolve to the left of the mantle array, but to a lesser extent than the Siberian samples that are characterized by the most negative θ values. Thus, the Siberian samples with the most unusual Ce-Nd isotopic compositions are the only group to plot close to the deep crust end-member calculated from classical mass-balance budget of the bulk silicate Earth. These results suggest that the lower crust sampled by Siberian xenoliths is only a minor component in the terrestrial deep crust. We use this database to estimate new parent/daughter ratios for the lower continental crust: $^{138}La/^{142}Ce = 0.00380 \pm 0.00007$ and $^{147}Sm/^{144}Nd = 0.128 \pm 0.007$. Measurements and models are finally reconciled when considering massive recycling of lower continental crust through Earth's history, totaling 3 to 4 present-day, continental crust masses.

KEYWORDS

Rare earth elements, ^{138}La-^{138}Ce, ^{147}Sm-^{143}Nd, lower continental crust recycling.

1. Introduction

The continental crust (CC) is a low-mass reservoir accounting for a large share of the highly incompatible elements in the silicate Earth. This share increases with greater incompatibility (preferential partitioning to the melt during magmatic processes) so that the CC concentrates 6 to 25% of the light rare earth elements (LREE: La to Nd) of the

bulk silicate Earth (BSE – using REE values from McDonough and Sun, 1995 and Rudnick and Gao, 2014). The upper continental crust (UCC) is the most accessible layer of the continental crust, and its average composition of refractory elements is essentially inferred from fine sediments such as loess and diamictites that sample large areas (McLennan, 2001). The REE compositions in these sediments reflect those of their sources because mechanical weathering has a negligible effect on these elements (Chauvel et al., 2014; Taylor and McLennan, 1981). While representing 70 wt.% of the total CC, the middle and lower continental crust (MCC and LCC) is much less characterized than the UCC. In particular, very few LCC sections are exposed tectonically, and LCC samples are mostly xenoliths in volcanic rocks and have essentially mafic compositions (<53 wt.% SiO_2). Most LCC samples are affected by granulite-facies metamorphism (±pyroxene, ±plagioclase feldspar, ±garnet, ±oxides) occurring at high-pressure – high-temperature conditions in the deep crust. The compositions of these deep crust reservoirs were estimated from mid-crustal rocks (e.g., MCC exposed in China – Gao et al., 1998), granulites exposed at the surface, and xenoliths (Bohlen and Mezger, 1989; Downes, 1993; Rudnick, 1992) together with geophysical constraints (Weaver and Tarney, 1984; and references therein). However, the heterogeneous nature of the deep CC has made it challenging to determine its average composition with certainty. The estimates vary between studies but all seem to agree on a more mafic composition for LCC than for MCC (Hacker et al. 2015; Rudnick and Gao, 2014).

This study provides the first measurements of the ^{138}La-^{138}Ce ($T_{1/2}$ = 292.5 Ga – Tanimizu, 2000) and ^{147}Sm-^{143}Nd isotope systems ($T_{1/2}$ = 106 Ga – Begemann et al., 2001) in deep crustal rocks. During melt extraction from the mantle, melting residues have lower La/Ce and higher Sm/Nd ratios than the melt because Sm and Ce are more

compatible than Nd and La, respectively (Hofmann, 1988). As a result, magmas extracted from initially melt-depleted reservoirs define a negative correlation in the ^{138}Ce-^{143}Nd isotopic space. The "εCe-εNd mantle array" has been precisely defined using a large number of isotope measurements of mid-ocean ridge basalts (MORB) and ocean island basalts (OIB – Israel et al., 2020; Willig and Stracke, 2019; Willig et al., 2020). The Ce-Nd isotopic composition of the UCC was defined from loess measurements in a previous study (Israel et al., 2020). Because the UCC plots on the εCe-εNd mantle array, the deep crust end-member calculated from mass-balance calculations in previous studies has negative εCe-εNd values (Israel et al., 2020; Willig and Stracke 2019; Willig et al., 2020). Like many studies that attempted to characterize large-scale reservoirs, they mainly base their assumptions on trace element compositions of these reservoirs reported in review studies. This approach is however biased due to large uncertainties on the mean concentrations and the absence of isotopic constraints. To address this, we explore the Ce-Nd isotopic composition of the deep continental crust by analyzing 35 middle to lower continental crust samples from three localities: (1) xenoliths of Permo-Triassic rocks in basaltic breccias from Neogene maars in Massif Central, France; (2) uplifted deep Permian crust from the Ivrea-Verbano zone, Italy, and (3) Neoarchean to Paleoproterozoic xenoliths from the Devonian Udachnaya kimberlite in the central Siberian craton, Russia. Our UCC dataset is complemented by new analyses of Precambrian composites from the Canadian shield. Our data are compared to a large dataset of REE contents in worldwide granulites to evaluate their significance in the lower crust budget. In particular, we investigate the distribution of $^{138}La/^{142}Ce$ and $^{147}Sm/^{144}Nd$ ratios in lower crust samples and their impact on the isotope evolution of the lower crust. The study of ^{138}La-^{138}Ce and ^{147}Sm-^{143}Nd isotopic systems in the deep crustal rocks offers a new perspective on

the REE composition of the continental crust. It brings new information to re-evaluate the long-term evolution of the continental crust.

2. Samples and methods

2.1. Geological context and sample description

Ivrea Verbano Zone, Italy

The five samples from the Ivrea-Verbano zone (IVZ – Alps) in northwestern Italy are the only samples in our set from tectonically exhumed deep crust (see Fig. 1 in Quick et al., 2003). They sample two major local lower crust units: the Kinzigite Formation (amphibolite to granulite-facies paragneiss) and the Basic Formation (mafic complex and lenses of mantle peridotite). The mafic complex results from underplating on, and intrusions of mafic magmas into, the base of the pre-existing crust (Quick et al., 1994; Voshage et al., 1990 – main magmatic phase dated at 288 Ma by U-Pb dating on zircons and monazites – Peressini et al., 2007; Voshage et al., 1990). It caused a perturbation of deep crust geotherms which delayed the Sm-Nd closure age by about 18 Ma (270 Ma in garnet-free mafic rocks – Downes, 1993). The magmatism favored the intra-crustal differentiation and drove metamorphic events in the lower crust (granulite and amphibolite facies) to upper crust conditions (greenschist facies - Schuster and Stüwe, 2008). Vertical uplift, crustal thinning, and lithosphere wedging during the Alpine collision (from late Paleozoic to early Mesozoic) are responsible for the ascent of the LCC to the surface (Handy et al., 1999) and for multiple high-temperature events that affected the MCC to LCC. The IVZ records a long-lasting, 300 Ma tectonic, metamorphic, and magmatic history that preserves its igneous structure (Langone et al., 2018; Peressini et al., 2007).

157 The rocks in this study are metabasite (IV1 – plagioclase-hornblende-clinopyroxene-
158 orthopyroxene), granulite-facies layered charnockite (IV5 – plagioclase-garnet-quartz-
159 hornblende), granulite-facies migmatite (IV9 – biotite-sillimanite-garnet-quartz) and
160 metapelite (IV10 – garnet-sillimanite-biotite). They have been affected by medium to
161 high-grade metamorphism and deformation.
162
163 *French Massif Central, France*
164 Three xenoliths from Bournac and eight xenoliths from Beaunit were analyzed during
165 the course of this study (Eastern French Massif Central – FMC – see Fig. 1 in Rossi et
166 al., 2006). In this locality, xenoliths from the upper crust to the shallow mantle were
167 brought to the surface during Miocene and Eocene explosive volcanic activity
168 (Féménias et al., 2004; Rossi et al., 2006). Zircons in metasedimentary granulites from
169 Bournac were dated between 150 and 630 Ma (Rossi et al., 2006). The oldest zircons
170 (>400 Ma) have a detrital origin and the youngest ones were formed by crustal
171 reworking in a lower crust environment during the Hercynian orogeny (See Rossi et al.,
172 2006 and references therein). Garnet-feldspar-whole rock Sm-Nd isochrons give an age
173 of 200 Ma in agreement with the age of the metamorphism (Downes et al., 1990).
174 The Beaunit maar is settled on the Permian Beaunit layered complex which was
175 emplaced at the crust-mantle transition at 257 Ma (U-Pb zircon age – Féménias et al.,
176 2003). This plutonic complex corresponds to a stratified intrusion located about 30 km
177 below the surface at the mantle-crust interface (Berger et al., 2007; Féménias et al.,
178 2003).
179 Bournac samples are the most felsic samples of our collection and all of them are felsic,
180 garnet-rich metasedimentary rocks (plagioclase-garnet-biotite-amphibole assembly).
181 Beaunit samples range from ultramafic plutonic amphibole-rich rocks (BPG2) to mafic

and felsic charnockites (B152). Mafic and ultramafic samples show no clear evidence of high-degree metamorphism or deformation, whereas two felsic samples (BG6 and B2-gneiss) show deformation and a mineralogical organization into bedding planes.

Udachnaya, Central Siberian craton, Russia

The fifteen samples from Siberia are xenoliths from the Udachnaya kimberlite pipe in the central Siberian craton (Markha terrane, East of the Anabar Province). Udachnaya is well known for its unaltered mantle and deep crustal xenoliths suitable for petrological and geochronological studies (Ionov et al., 2010; Moyen et al., 2017). The host kimberlites were dated at ca. 360 Ma (Kinny et al., 1997).

The age and origin of the crust beneath the Anabar province are still a matter of debate. The CC formation involved two major events: (1) the first at 2.7–3.0 Ga (Moreira et al., 2023; Moyen, 2017) and (2) the second at 1.9-1.8 Ga (U-Pb dating on zircons – Moreira et al., 2023; Moyen et al., 2017; Shatsky et al., 2019) by plume upwelling, underplating of basaltic magmas. Moyen et al. (2017) and Moreira et al. (2023) argued that the LCC was strongly affected by a rejuvenation event at 2.0–1.8 Ga, whereas the MCC and UCC remained largely unaffected after their formation at 2.7 Ga. Shatsky et al. (2018, 2019) suggested that the 1.8 Ga-old juvenile materials are also present in the LCC and the UCC. These studies suggest that Paleoproterozoic delamination and rejuvenation of the lower Archean lithosphere had major effects on the structure and composition of the continental crust in the Anabar province (Moyen et al., 2017). The craton remained then thermally undisturbed since 1.8 Ga.

All 15 Udachnaya samples, collected at depths over 400m in the open mine, consist of fresh minerals and have no eruption-related or alteration materials. Six most mafic samples (246-17, 1003-14, 1010-13, 226-03, 232-17, and 360-13) are rich in garnet,

clinopyroxene, and plagioclase (± amphibole) and thus equilibrated at amphibolite to granulite facies conditions. They likely represent the deepest parts of the crust. Sample 1001-16 is a picritic gabbro mainly composed of olivine, pyroxene, and amphibole; sample 1006-14 is a mantle-like olivine-pyroxenite. All the other samples have more felsic mineral assemblages, from amphibole-rich granitoid to felsic granulite. Three of them contain abundant feldspar (370-13, 1014-14, and 98-13). 85% of the samples have more than 40 wt.% plagioclase according to their CIPW norm.

Canadian Precambrian Shield, Canada

Lastly, we analyzed four composite samples from the Canadian Precambrian Shield. Shaw et al. (1967; 1976) prepared the composite samples to estimate the major- and trace-element composition of the Canadian Precambrian shield. They were derived by sampling rocks across broad geographic regions of Canada, and composite powders were made from 122 rocks from Northern Quebec (NQ), 116 from Baffin Island (BI), 18 from Saskatchewan (SS), and 116 from Southwestern Quebec (SQ). These provinces have ages ranging between 0.9 and 2.7 Ga (McCulloch and Wasserburg, 1978).

2.2. Analytical methods

Sample preparation

All Phanerozoic samples (from IVZ and FMC) were cut with a rock saw and crushed in Laboratoire Magmas and Volcans (LMV), Clermont-Ferrand, France. Precambrian xenoliths from Udachnaya were cut and crushed at Montpellier University, France. To avoid contamination by the host lava, the rims (one centimeter) of each xenolith (initially 5 to 15 cm large) were removed, including veins inside the xenoliths (due to

232 possible kimberlite interaction or fluid percolation). The Canadian composite samples
233 were provided in powder form (Shaw et al., 1967, 1976). The IVZ and FMC samples
234 were processed and analyzed for major elements at the LMV using a Jobin-Yvon
235 ULTIMA C® ICP-AES and alkali fusion procedure, whereas analyses of the Siberian
236 samples were made by XRF analyses of beads produced by fusion of rock powders with
237 lithium-metaborate at the University of Mainz, Germany. Major- and trace-element
238 compositions of the Canadian samples were reported by Shaw et al. (1967, 1976), and
239 the compositions are nicely matched by new data reported here (see below).
240
241 Between 50 to 800 mg of sample powders were first acid-digested using a 3:1, 65% HF
242 / 48% HNO_3 mixture maintained at 75 °C on a hot plate for 48 hours. Once dried they
243 underwent a second step of digestion with 6M HCl, before breaking down fluorides by
244 three dissolutions with 1:1, 48% HNO_3 / 6M HCl, and slow evaporation at 70 °C.
245 Refractory mineral-rich samples were then re-digested in a concentrated 10:1, HF /
246 HNO_3 mixture using Teflon® vessels that were placed within Parr® bomb apparatus (48
247 hours at 180 °C), or in double distilled NH_4HF_2 (crystal form) within Savillex® beakers
248 (48 to 72 hours at 220 °C). Once dried they again underwent a 6M HCl digestion. Once
249 dissolved, a small portion (1%) of the solution was aliquoted for trace element and
250 La/Ce ratio measurements.
251
252 Cerium and Nd were separated following procedures described by Garçon et al. (2018),
253 Bonnand et al. (2019) and Israel et al. (2020). Using the AG50W-X8 resin, the major
254 elements were eluted in 2.5M HCl and Ba in 2M HNO_3 before collecting the REE
255 fraction in 6M HCl. The REE fraction was processed in Ln-Spec resin (50-100 mesh)
256 using an oxidation technique (20mM $NaBrO_3$ / 10M HNO_3) to oxidize Ce (tetravalent)

while eluting the other trivalent REE; then the Ce fraction was collected by reducing the environment (20mM H_2O_2 / 6M HCl). The Ce fraction was purified in a final step using AG50W-X8 (200-400 mesh, 1 ml) to remove residual Na, Br and Ba. Similarly, the REE fraction was purified before it was processed using Ln-Spec resin to isolate Nd. Mean procedural blanks for Ce and Nd were 113 pg and 14 pg, respectively.

Mass spectrometry

Trace-element abundances were measured with the LMV Agilent 7500® quadrupole ICP-MS instrument in collision cell mode. Concentrations were calculated using an external calibration (CMS reference material, Inorganic Venture) and the associated errors are about 2-6% (2sd) for REE and up to 28% for Li, Sr and Ba. Certified USGS reference materials BHVO-2 and BCR-2 were analyzed with our samples to assess the accuracy of our analytical protocol. Our results for BHVO-2 and BCR-2 differ from accepted reference concentrations (Jochum et al., 2016) by less than 10% for REE. Errors calculated from ratios are significantly reduced and we obtained a reproducibility of 1% on 7 repeated measurements of the CMS standard solution (2sd). A distinct analytical session was dedicated to the measurement of La/Ce ratios. They were estimated using a calibration curve defined from four gravimetrically prepared standards with different La/Ce ratios (0.2681, 0.3712, 0.5703, 0.7878) produced from CMS elementary standards. The reproducibility errors calculated from three repeated measurements of the four standards are ≈0.3% (2sd).

Cerium isotope ratios were measured in oxide form on a ThermoScientific Triton Plus® TIMS at LMV, using a static mode method and double 99.99% Re filaments (Bonnand et al., 2019). Oxygen correction, correction for mass-discrimination using $^{136}Ce/^{142}Ce = 0.01688$, and correction for the tailing effect due to the overabundant signal of

$^{140}Ce^{16}O$ affecting $^{136}Ce^{16}O$ and $^{142}Ce^{16}O$ signals (extrapolation from half-masse measurements – details for corrections are given in Bonnand et al., 2019) were performed offline. The mass fractionation of the CeO^+ beam is assumed to follow an exponential law. Uncertainties reported below are 2 standard deviations. Cerium isotope measurements of this study were acquired during three distinct sessions. The mean tailing correction was equal to $\Delta\varepsilon Ce = 1.01 \pm 0.25$ (n = 73, samples and standards). Repeated measurements of our Ce_{LMV} synthetic reference material gave $^{138}Ce/^{142}Ce$ = 0.02257036 ±74 (33 ppm; n = 24). All $^{138}Ce/^{142}Ce$ ratios measured in samples and rocks standards are normalized to the Ce_{LMV} value $^{138}Ce/^{142}Ce = 0.002257063$ (Israel et al., 2020 – $^{138}Ce/^{142}Ce_{CeLMV}$ / $^{138}Ce/^{142}Ce_{CeAMES} = 0.999835$). $^{138}Ce/^{142}Ce$ ratios measured for BCR-2 and BHVO-2 are 0.02256694 ±92 (41 ppm, n = 3) and 0.02256465 ±71 (31 ppm, n = 6), respectively.

Neodymium isotope ratios were measured on a ThermoScientific Triton® TIMS at LMV during three analytical sessions, using either a one-line or a two-line method and double 99.999% Re filaments. Mass discrimination was corrected using an exponential law and $^{146}Nd/^{144}Nd = 0.7219$. Measured $^{143}Nd/^{144}Nd$ ratios for the JNdi-1 standard reference material and the two rock samples BCR-2 and BHVO-2 are 0.512108 ±7 (15 ppm; n = 21), 0.512619 ±9 (18 ppm, n = 3), and 0.512972 ± 9 (15 ppm, n = 2), respectively. Since the JNdi-1 values increased during the three sessions, $^{143}Nd/^{144}Nd$ ratios of the analyzed samples and rocks standards were normalized to the JNdi-1 reference value of Garçon et al. (2018), i.e., $^{143}Nd/^{144}Nd = 0.512099$.

3. Results

3.1. Major and trace element compositions

Major and trace element compositions measured in this study are reported in Supplementary data 1. All metaigneous and metasedimentary samples in our study are presented on a total alkali (Na_2O+K_2O) *versus* silica diagram and compared with literature granulites (Fig. 1).

Samples from Bournac and Canada have the highest SiO_2 content, with values ranging from 58 to 71 wt.%. Ivrea and Beaunit samples are highly variable in SiO_2 (32 to 68 wt.% and 44 to 62 wt.%, respectively) but they contain the most mafic samples of our dataset (BPG2 and IV9). Siberian samples have 47 to 55 wt.% SiO_2 with one exception (62 wt.%). The more felsic samples show high Na_2O+K_2O values (up to 9.5 wt.%, SiO_2 = 53 wt.%). Loss on ignition (LOI) values in the Siberian samples range from 0.1 to 2.4 wt.%, with the highest values measured in samples that show veins, re-crystallization, or altered feldspar (322-13, 370-13 and 386-13). All the other samples have LOI lower than 0.86, with LOI attributed to the presence of primary hydrous minerals (biotite, amphibole). No clear correlation can be observed with any major or trace elements sensitive to alteration (e.g., Sr) or La/Ce and Sm/Nd ratios. LOI values of the West European samples range from 0.1 to 1 wt.%.

Bulk-CC normalized REE patterns (Fig. 2) show LREE depletions to LREE enrichments, as indicated by the moderate to high $La/Yb_{Bulk\ CC}$ ratios (where the subscript "Bulk CC" stands for ratio normalized to the bulk continental crust from Rudnick and Gao, 2014 – $La/Yb_{Bulk\ CC}$ = 0.30 – 4.9; except IV1, 246-17, B4g-lite and 370-13 samples that show $La/Yb_{Bulk\ CC}$ = 0.07, 0.13, 0.18 and 12, respectively).

The Siberian samples show the largest range of REE fractionation with $La/Yb_{Bulk\ CC}$ ratios varying from 0.13 to 12, which is a great range compared to West European samples ($La/Yb_{Bulk\ CC}$ = 0.07 – 4.0). For better visualization, Siberian samples are

presented in two diagrams (Figs. 2b,d) based on their Sm/Nd ratio. All the samples with a Sm/Nd>0.24 are mafic (SiO_2<50 wt.%) and contain garnet in their mineral assemblage. Thirteen Siberian samples show a moderate to high depletion in LREE compared to the MREE ($La/Gd_{Bulk\ CC}$ / $Gd/Yb_{Bulk\ CC}$ = 0.08 to 0.63 *vs.* 1.14 and 3.73 in 1014-14 and 370-13, respectively - Figs. 2b,d). Most of them show no significant cerium anomaly and a small negative europium anomaly (Ce/Ce* = 0.81 – 1.09 and Eu/Eu* = 0.58 – 0.98, where $Ce/Ce^* = Ce_N/(0.5\times(La_N+Nd_N))$ and $Eu/Eu^* = Eu_N/(0.5\times(Sm_N+Gd_N))$ where the subscript "N" stands for concentration normalized to CI chondrite – Barrat et al., 2012). Samples 98-13, 370-13 and 1014-14 have positive Eu anomalies (Eu/Eu* = 4.38, 1.35 and 1.27) consistent with their strong enrichment in feldspar, and they show a strong depletion in HREE compared to the other Siberian samples (Fig. 2d). Among them, only 370-13 has a high LOI of 2.4 (*vs.* 0.2 and 0.6 for 98-13 and 1014-14, respectively). All the other Siberian samples have LOI ranging between 0.1 and 1.4, except 322-13 whose LOI is 2.3.

3.2. ^{138}La-^{138}Ce and ^{147}Sm-^{143}Nd systematics

Measured Ce and Nd isotopic compositions are given in Table 1 and reported in epsilon (ε) notation in Figure 3. Most of the data for FMC, IVZ and Canadian samples plot within or very close to the Ce-Nd mantle array (for the FCM and IVZ samples εCe = -0.65 to 3.83 and εNd = -14.72 to 6.73; for Canadian samples εCe = 0.02 to 2.71 and εNd = -30.69 to -6.19). Bournac xenoliths, Ivrea samples and Canadian composites are located at the end of the mantle array toward the most radiogenic Ce and the least radiogenic Nd isotopic compositions, except BOU3 which plots to the right of the mantle array. Because the three Bournac samples have very similar Nd isotopic

compositions, the Ce isotopic composition of this sample seems anomalously radiogenic. Beaunit xenoliths range between the MORB and loess endmembers defined in Israel et al. (2020), in agreement with their large range of SiO_2 contents.

The Siberian samples mostly plot to the left of the mantle array in the εCe-εNd diagram. They cover a wider range of εCe values than FMC and IVZ samples, with εCe values from -1.75 to 5.78 for and εNd from -41.61 to -4.69. They define two nearly horizontal sub-parallel trends, with slopes distinct from that of the mantle array. The Siberian samples are reported in $^{138}La/^{142}Ce$-$^{138}Ce/^{142}Ce$ and $^{147}Sm/^{144}Nd$-$^{143}Nd/^{144}Nd$ diagrams (Fig. 4). They define a single regression line for each isotope system. Our data agree with literature ^{147}Sm-^{143}Nd data on granulites from the same area (Fig. 4b) but regressions are not sufficiently well defined to provide robust information on ages and form errorchrons (MSWD>10). The La-Ce errorchron age is nevertheless significantly younger than that for the Sm-Nd system (1.8 ±0.4 Ga and 2.7 ±0.3 Ga, respectively – calculated with IsoplotR – Vermeesch, 2018 – Fig. 4). These two ages are consistent with the chronology established using other methods. For example, U-Pb ages measured on zircons from both Udachnaya and Obnazhennaya kimberlites defined two peaks at 1.8 and 2.7 Ga (Moyen et al., 2017), which are similar to the U-Pb zircon ages from granulites of the Anabar province (Koreshkova and Downes, 2021; Moreira et al., 2023) and the Re-Os depletion ages of peridotite xenoliths from these pipes (Ionov et al., 2015a, 2015b). This is consistent with a common history for the lithospheric mantle and deep crust of the Siberian craton.

Isochron diagrams are not presented for Beaunit, Bournac and Ivrea samples. They are too young to extract relevant information from long-lived systems.

4. Discussion

4.1. Data from this study compared to crustal reservoirs

Recent publications, such as Rudnick and Gao (2014) and Hacker et al. (2015), provided estimates for the chemical composition of the deep crust. These compositions differ due to the relative weight given to measurements (e.g., abundance of mafic and felsic components) and geophysical constraints. Figure 1 reports the SiO_2 and alkalis for these reference compositions but also a large literature dataset composed of Archean and post-Archean granulites (grey and pink squares in Fig. 1).

The crustal samples in this study range from ultramafic to felsic compositions as shown in Figure 1 and fall within the range defined in the literature. The Siberian xenoliths from this study fall within the range of those reported by Koreshkova et al. (2011), Moyen et al. (2017) and Shatsky et al. (2019, 2018). However, they are more enriched in alkalis than most of the literature samples for similar SiO_2 contents, suggesting that this is typical of the Siberian craton. Samples 1001-16, 1014-14 and 370-13 have the highest Na_2O+K_2O (7.8, 7.0 and 9.5 wt.%, respectively), beyond the compositions commonly observed in literature lower crust samples (Figure 1).

Koreshkova et al. (2011) and Moyen et al. (2017) grouped Siberian xenoliths based on HREE/LREE ratios and K_2O that were unrelated to LOI. Koreshkova et al. (2011) suggested that most of the xenoliths in their study (collected in other parts of the kimberlite pipe than those in this study) were modified by interaction with kimberlite magmas, resulting in enrichments in LILE. Many of their samples were also modified by post-eruption processes such as alteration and interaction with fluids mobilized from local sedimentary country rocks. Since kimberlites are low in alkalis (Kamenetsky et al., 2012) and strongly enriched in LREE relative to HREE ($La/Yb_{Bulk\ CC}$ = 14 to 20), contamination by a kimberlitic melt for our samples can be ruled out. This process

cannot explain the relative depletion in LREE relative to HREE in the Udachnaya xenoliths ($La/Yb_{Bulk\ CC}$ = 0.13 to 1.8; except samples 1014-14, 1001-16 and 370-13 with $La/Yb_{Bulk\ CC}$ = 3.1, 4.9 and 12, respectively – Fig. 2b,d). Moreover, our samples plot far from Udachnaya kimberlites on the Sm-Nd errorchron diagram whereas contamination by the host kimberlite is clearly identified for one xenolith analyzed by Koreshkova et al. (2011) (Fig. 4b). Therefore, the Ce-Nd isotopic compositions of the Siberian xenoliths are unlikely to be affected by kimberlite contamination.

4.2. Ce-Nd isotopic evolution of crustal samples

The isotopic composition of rocks evolves with time as a function of their parent/daughter ratios. Figure 5 shows the initial isotopic compositions of the samples from this study based on their measured parent/daughter ratios and published ages. The initial isotopic composition is unrelated to this discussion, and we focus here on the evolution paths of the samples, represented as arrows from initial to present-day isotopic compositions.

The majority of the Phanerozoic samples from the FMC and the IVZ evolve along the Ce-Nd mantle array. Because these samples are young, both their present-day and initial isotopic compositions are close to each other in the εCe-εNd diagram (Fig. 5a). In contrast, the much older Canadian and Siberian samples plot to the left of the mantle array (Fig. 5b). While the age and thermal history of the Canadian samples are uncertain due to their composite nature, their epsilon values plot close to the mantle array after recalculation back to 3 Ga (maximum presumed age of the sampled terrains – Fig. 5a). Their evolution paths are close to the slope of the mantle array, creating a slight deviation from the mantle array integrated over 3 Ga. Using younger ages for correction

does not affect their evolution paths and results in similar conclusions. The isotopic compositions of the Siberian samples also move closer to the mantle array (Fig. 5b) when back-calculated up to 2.7 Ga (Moyen et al., 2017), except sample 370-13 that moves further from the mantle array. This sample has the highest LOI value and it contains altered feldspar suggesting alteration affected its La/Ce ratio. The evolution paths of the Siberian samples are much steeper than the slope of the mantle array. However, previous results suggest the Siberian crust formed during the Archean at ~2.7 Ga flowed by a major event of delamination and rejuvenation at 1.8 Ga (Moyen et al., 2017; Shatsky et al., 2019), which is consistent with chronological insights from La-Ce and Sm-Nd systematics (Fig. 4). The disturbance of the La-Ce systematics in the Siberian samples at 1.8 Ga suggest their evolution paths are probably not linear but should be subdivided into at least two segments in Figure 5b.

The observed depletion in LREE relative to MREE and the disturbance of the La-Ce systematics in the Siberian samples at 1.8 Ga suggest high-grade metamorphism may have affected the entire crustal section (Fig. 2) and produced a decrease in the La/Ce ratios. The La-Ce system is more prone to disturbances during fluid circulation accompanying the metamorphism than the Sm-Nd system because the REE mobility decreases with increasing atomic number. Remarkably, lanthanum appears to be the most mobile REE during fluid interaction in granulite facies (e.g., dehydration of amphibole – Ague, 2017 and references therein). Cerium changes valence from 3+ to 4+ under oxidizing conditions and thus is decoupled from other REE, as seen in modern seawater and chemical marine sediments (Bau, 1999). The percolation of an oxidized fluid may reduce cerium mobility relative to other REEs, although this is not documented in the literature at LCC conditions. Therefore, a decrease in the La/Ce

457 ratios in Siberian samples is more likely due to the higher mobility of La during high-
458 grade metamorphism.
459
460
461 4.3. Deviation from the εCe-εNd mantle array: comparing our data with literature
462 The isotopic evolution of samples is usually compared by calculating their $f_{P/D}$
463 parameter (Vervoort et al., 2000), where $f_{P/D}$ represents the deviation of the
464 parent/daughter ratio of a sample from this ratio in a chondritic reservoir. The values
465 for $f_{Sm/Nd}$ and $f_{La/Ce}$ can be either positive or negative and indicate the direction and
466 amplitude of the isotopic evolution relative to CHUR in an epsilon-epsilon diagram
467 (Fig. 5c). The ratio F = $f_{Sm/Nd}$ / $f_{La/Ce}$ integrates the effects of both $f_{Sm/Nd}$ and $f_{La/Ce}$. This
468 parameter is relevant for quantifying the deviation from the CHUR as a point but not
469 from the mantle array line on epsilon-epsilon diagrams. As a handy alternative, we
470 compare the evolution vectors of the samples with the vector formed by the mantle
471 array trend (Fig. 5c). These vectors are distinct by the oriented angle θ calculated on an
472 orthonormal epsilon-epsilon diagram. Samples with evolution vectors to the left of the
473 mantle array will exhibit negative θ values (Fig. 5c). The rate of deviation of the
474 samples from the mantle array is also calculated in the form of the horizontal deviation
475 of the Ce isotopic composition over a billion-year period (ΔεCe/Ga – Fig. 7a). Both θ
476 and ΔεCe/Ga parameters only depend on the La/Ce and Sm/Nd ratios of a sample.
477 Disregarding isotopic or age constraints, θ and ΔεCe/Ga provide quantitative insights
478 into how samples diverge from the mantle array with time, indicating the direction (≈
479 degree of decoupling of La/Ce and Sm/Nd ratios) and rate of deviation per time unit,
480 respectively (calculations detailed in the Supplementary material). These parameters
481 calculated for our samples are reported in Supplementary data 2).

The evolution vectors of the West European samples display slopes that diverge slightly from the mantle array, with θ values ranging from -4.0 to +3.0° (Fig. 7a), except sample BOU2 showing a higher θ value at +5.6°. While it also slightly deviates from the mantle array, IV1 evolves upward (θ = -176). The Canadian composites have slightly negative θ values from -2.3 to -3.9°. SQ has a higher θ value (-7.8°) but it also shows a much younger Nd model age than the other Canadian samples (T_{DM} = 1 Ga *vs.* T_{DM} = 2.1-2.5 Ga – details are given in Supplementary data 1), suggesting a late disturbance. The Siberian samples from this study and the literature have a large range of θ values, and most of them are strongly negative (down to -21.0°), except two samples with the highest La/Ce ratios (1014-14 and 370-13 with θ = -0.5 and +2.8°, respectively).

While the samples from Europe mostly show ΔεCe/Ga between -0.7 and 0.5, and Canadian samples between -1.5 and -0.5. Siberian samples deviate more significantly from the mantle array with ΔεCe/Ga from -2.3 to -0.3 (except 1014-14 and 370-13 with ΔεCe/Ga = -0.1 and 0.8, respectively).

To further explore the significance of our data and inferences, and how representative the Siberian xenoliths could be of the CC, we calculated θ and ΔεCe/Ga values using the elemental concentrations of 445 Archean and 1136 post-Archean granulites from the literature. We used the database compiled by Hacker et al. (2015) and added new values from the PetDB database. Figure 6 presents the relative numbers of samples from each region for the Archean and post-Archean datasets. All cratons are incorporated into both the Archean and post-Archean datasets. Compared to the global ages distribution of the continental lithosphere (Fig. 7 in Poupinet and Shapiro, 2009) our database shows an under-representation of post-Archean samples from Siberia relative to their Archean equivalents and an over-representation of West European samples

507 relative to Antarctica, Australia and South America that are under-represented. The
508 calculated θ and ΔεCe/Ga values of the complete database are reported in
509 Supplementary data 2 and shown in Figure 7a. Archean and post-Archean granulites
510 present similar, normal distributions of θ and ΔεCe/Ga values with peaks at -3° and -
511 0.4, respectively. These slightly negative values will result in isotopic compositions
512 increasingly deviating to the left of the mantle array over time. When all data are plotted
513 in a θ *versus* ΔεCe/Ga diagram, a positive correlation is observed. The linear regression
514 is defined by the equation ΔεCe/Ga = 0.15 (±0.03) × θ -0.01 (±0.05). For θ = -3°, it
515 intercepts ΔεCe/Ga = -0.46 ±0.05, consistent with the peak of ΔεCe/Ga. We note that
516 the Siberian xenoliths have strongly negative θ and ΔεCe/Ga values (Fig. 7a) which are
517 found among the most extreme values documented for granulites in the literature.
518 The θ and ΔεCe/Ga values calculated from reference compositions of the LCC
519 (Rudnick and Gao, 2014 and Hacker et al., 2015 – mafic and felsic models) are more
520 negative than the distribution peaks of literature granulites (θ = -6.6 to -5.6°; ΔεCe/Ga
521 = -1.1 to -0.6). According to these reference compositions, the LCC should deviate
522 significantly from the mantle array with time, to a greater extent than most granulites,
523 but significantly less than the Siberian xenoliths.
524
525
526 4.4. La/Ce and Sm/Nd ratios of the lower crust
527 To better understand the relative influence of the parent/daughter ratios on the θ values
528 of the Siberian samples and literature granulites, their present-day $^{138}La/^{142}Ce$ and
529 $^{147}Sm/^{144}Nd$ ratios are plotted in Figure 7b, together with their frequency distribution
530 histograms. Siberian samples have lower $^{138}La/^{142}Ce$ values (maximum distribution at
531 0.0033) than other granulites that show distribution peaks at 0.0035 and 0.0039 for

532 Archean and post-Archean granulites, respectively, with a larger range for Archean
533 samples. Post-Archean granulites have a normal $^{147}Sm/^{144}Nd$ distribution with a peak
534 at 0.125, while Archean granulites show a flatter distribution. Siberian samples also
535 show a wide range of $^{147}Sm/^{144}Nd$ ratios without clear peaks.
536
537 Two regression lines intersect the CHUR composition in Figure 7b. The first one
538 represents parent/daughter ratios for samples with isotopic compositions that evolve
539 along the mantle array ($\theta = 0°$ – black line) and the other one with an angle $\theta = -3°$
540 (purple line) corresponds to the peak value in the histogram of Figure 7a. The
541 distribution of the parent/daughter isotope ratios of granulites in the histograms of
542 Figure 7b raises questions about the LREE concentrations of the LCC. Parent/daughter
543 ratios obtained using reference compositions do not plot on the $\theta = -3°$ line nor the
544 mantle array line. Their $^{147}Sm/^{144}Nd$ ratios range from 0.113 to 0.154 (Rudnick and
545 Gao, 2014 and Hacker et al., 2015 – see Supplementary data 2), encompassing a
546 significant portion of granulite compositions. The peak of $^{147}Sm/^{144}Nd$ observed in
547 granulites is however close to a mafic composition of the LCC, between the felsic and
548 mafic composition models of Hacker et al. (2015). Their $^{138}La/^{142}Ce$ ratios range from
549 0.00350 to 0.00322, in agreement with the peak for Archean granulites but lower than
550 the peak observed for post-Archean granulites (Figure 7b).
551 Our observations are based on a comprehensive set of granulite compositions, however,
552 weighting the parent/daughter ratios by the relative surface area of different continents
553 is unlikely to change significantly our observations. In any case, a more mafic LCC
554 than the Rudnick and Gao (2014) reference is suggested by the literature on granulites.
555 The granulite database (Fig. 7) indicates the most likely parent/daughter ratios of the

556 LCC that result in θ = -3° and ΔεCe/Ga = -0.46 ±0.05 are $^{138}La/^{142}Ce$ = 0.00380
557 ±0.00007 and $^{147}Sm/^{144}Nd$ = 0.128 ±0.007.
558
559 The atypical isotope evolution of Siberian samples likely results from La/Ce
560 decrease due to enhanced mobility of LREE during high-grade metamorphic conditions
561 (granulite facies – Ague, 2017). However, generalizing this conclusion to all Archean
562 granulites from the literature may be oversimplistic since it is difficult to assess which
563 parent/daughter ratio has greater effects on their isotope evolution. Shifting
564 parent/daughter ratios from the mantle array line to the -3° line can be achieved either
565 by decreasing the $^{138}La/^{142}Ce$ or $^{147}Sm/^{144}Nd$ ratio by ≈11 % and 18%, respectively,
566 which are both plausible. Such decreases may be caused by partial melting of crustal
567 material, fractional crystallization or metamorphism generating inhomogeneous
568 enrichment or depletion in the REE pattern in lower crust conditions. Both ratios may
569 even decrease simultaneously during metamorphism involving fluid-rock interaction,
570 alteration, or incorporation of hydrothermally-related material or altered sediments in
571 the melt (tetrad effect – Lee et al., 2010 and reference therein).
572
573
574 4.5. Evidence for massive recycling of lower continental crust
575 *The continental crust in the mass-balance budget of the bulk silicate Earth*
576 The composition of the bulk silicate Earth (BSE) can be expressed as the
577 complementarity of the CC and depleted MORB mantle (DMM), i.e. BSE = CC +
578 DMM (Allègre and Lewin, 1989). Mantle geochemists have emphasized the
579 importance of recycling oceanic crust (OC) throughout Earth's history to understand
580 the present-day composition of the convecting mantle and the signification of the

581 mantle array (Stracke et al., 2003). While it represents only a small fraction of the crust
582 (3-30 wt.%), the OC was subducted over geologic time and its current share in the
583 mantle is difficult to constrain. Moreover, the REE content of the OC is about four
584 times lower than in the LCC (White and Klein, 2014) and the calculated Ce-Nd isotopic
585 composition of the OC evolves very slightly with time and remains on the mantle array
586 (see Figure 2 in Willig et al., 2020). The bulk OC is then supposed to have little impact
587 on the mass-balance budget of Ce and Nd in the BSE.
588 The mass-balance budget of the BSE was estimated by Israel et al. (2020) using the
589 measured Ce-Nd isotopic composition of the DMM and reference isotopic
590 compositions and Ce and Nd contents for the BSE and CC (Table 2; Supplementary
591 material – details about the input parameters are given in Israel et al., 2019). The
592 calculated Ce-Nd isotopic range for the bulk CC (orange field in Fig. 8) is located to
593 the left of the mantle array and is distinct from the UCC estimates based on mean loess
594 values. As a result, the deep continental crust (MCC+LCC) must plot even further to
595 the left of the mantle array, in the negative εCe-εNd quadrant (grey field in Fig. 8) to
596 fulfill the complementarity bulk CC = UCC + (MCC+LCC). Willig and Stracke (2019)
597 and Willig et al (2020) showed similar results for their modeled LCC. The horizontal
598 distances (ΔεCe) of the bulk CC and the deep continental crust from the mantle array
599 are -1.5 ±0.8 and -2.9 ±1.2, respectively (mean values and two standard deviations).
600 These estimates consider: (1) three reference compositions of the CC after Rudnick and
601 Gao, 2014 and Hacker et al., 2015 and (2) the range of Nd isotopic composition of the
602 bulk CC – εNd = -21 to -10 after Allègre and Lewin, 1989 and Chauvel et al., 2014,
603 respectively). Only the Ce-Nd isotopic compositions for the Siberian samples plot near
604 the modeled MCC+LCC reservoir. The peak θ values in the literature dataset (-3°, Fig.
605 7a) and the associated ΔεCe per billion years, enable to estimate the deviation of the Ce

606 isotopic composition from the mantle array for the LCC at about -0.8 to -1.1, for a mean
607 age of the CC between 1.8 and 2.4 Ga (Chauvel et al., 2014; Taylor and McLennan,
608 1995). The LCC is then potentially much less distant from the Ce-Nd mantle array than
609 the MCC+LCC reservoir calculated from the mass-balance budget (Fig. 8).
610 The mass fraction of bulk CC relative to the BSE ($m_{bulk\ CC}/m_{BSE}$ = ($^{143}Nd/^{144}Nd_{BSE}$-
611 $^{143}Nd/^{144}Nd_{DMM}$) / ($^{143}Nd/^{144}Nd_{CC}$-$^{143}Nd/^{144}Nd_{DMM}$) × $[Nd]_{BSE}/[Nd]_{CC}$) can be estimated
612 using a mass-balance budget, and is calculated to be 0.026 ±0.013. However, the mass
613 fraction of the present-day CC relative to the mantle ($m_{present\text{-}day\ CC}/m_{present\text{-}day\ mantle}$ =
614 0.006: $m_{present\text{-}day\ CC}$ = 2.367×10^{25}g and m_{mantle} = 4.007×10^{27}g – Lodders and Fegley,
615 1998) is 4.4 times lower than the fraction estimated from the BSE mass-balance. Thus,
616 about 3.4 times the present-day mass of the continental crust may have been recycled
617 to the mantle, which is larger than recent estimates of 1–1.6 times the present-day mass
618 of CC (e.g., Dhuime et al., 2018; Kumari et al., 2016).
619 While these calculations imply a chondritic BSE, two recent studies have provided
620 compelling evidence that the BSE (or primitive mantle) is slightly depleted in
621 incompatible elements relative to chondrites (Frossard et al., 2022; Johnston et al.,
622 2022). Recent mass balance models have also reevaluated the global crust-mantle
623 differentiation of the Silicate Earth and propose the existence of an early depleted
624 reservoir (EDR) formed prior to the extraction of the continental crust (Hofmann et al.,
625 2022). To reconcile a 7.9 ppm excess in ^{142}Nd compared to chondrites (Frossard et al.,
626 2022), we consider a 2.65% higher Sm/Nd ratio than chondrites ($^{147}Sm/^{144}Nd_{EDR}$ =
627 0.2012) and we reevaluate the LREE content of this EDR. Based on a 4.568 Ga
628 formation age, we estimate that the present-day values for the primitive mantle are
629 $^{138}La/^{142}Ce_{EDR}$ = 0.00306, εCe_{EDR} = -0.3, and εNd_{EDR} = 3.1. With these new parameters,

630 the mass fraction of bulk CC relative to the BSE is lower than for a chondritic BSE
631 ($m_{bulk\ CC}/m_{BSE}$ = 0.016 ±0.008) and corresponds to 2.7×$m_{present\text{-}day\ CC}/m_{present\text{-}day\ mantle}$.
632
633 *Impact of lower continental crust recycling on the mass-balance budget of the BSE*
634 Tang et al. (2015) suggested that Eu anomalies in the UCC, MCC and LCC cannot be
635 explained without considering a greater proportion of the LCC than the proportion
636 observed in the present-day CC. They suggested different relative proportions of the
637 different sub-reservoirs of the CC with the LCC representing 84 wt.% rather than the
638 10% recommended by Rudnick and Gao (2014). This implies that 88 wt.% of the LCC
639 was recycled to the mantle, and represents about 2.9×$m_{present\text{-}day\ CC}$. The UCC and MCC
640 would then represent only 8 wt.% and 8 wt.%, respectively, of the bulk CC (*vs.* 32 wt.%
641 and 30 wt.%, respectively, according to Rudnick and Gao, 2014).
642 The massive recycling of LCC proposed by Tang et al. (2015) affects the mass-balance
643 calculations for the Ce-Nd systematics. The resultant bulk CC and MCC+LCC εCe-
644 εNd isotopic compositions are closer to the mantle array than the previous reservoir
645 estimates (with ΔεCe ranging from -1.2 to -1.6 (±0.9) – see bulk CC and MCC+LCC
646 represented as red and black fields in Fig. 8). The MCC+LCC reservoir fits with the
647 granulite database, suggesting that the Ce-Nd isotopic composition of the LCC is
648 located to the left of the mantle array, but not as far as the Siberian samples. Our
649 estimates indicate a mass fraction of bulk CC relative to the BSE ($m_{bulk\ CC}/m_{BSE}$ = 0.024
650 ±0.011 and 0.033 ±0.022 for depleted and chondritic BSE, respectively) that is 4.1 to
651 5.6 times higher than the mass fraction of the present-day CC. Consequently, we
652 suggest that 2.6 to 3.9×$m_{present\text{-}day\ CC}$ of LCC was recycled in the mantle during Earth's
653 history (total of 3.1 to 4.6×$m_{present\text{-}day\ CC}$ of CC was recycled in the mantle, including 84
654 wt.% of LCC).

Continental growth models remain challenged by the difficulty in measuring the rates of formation and destruction of the continental crust through time (e.g., Dhuime et al., 2018; Kumari et al., 2016; Reimink et al., 2023; Rosas and Korenaga, 2018). Our study suggests a large amount of crustal recycling, since we estimated that the portion of CC derived from the Earth's mantle is four to five times larger than the current mass of CC, and most of the recycled crust is from its deepest mafic part. Geological processes, such as crustal delamination, play a crucial role in explaining this substantial LCC recycling while considering the contemporary structure of CC.

In this context, Hacker et al. (2011, 2015) have highlighted that the lowermost mafic crust can become unstable and detach, sinking into the mantle beneath rifts and volcanic arcs. Particularly during subduction, the densest mafic crust descends into the mantle while some of the silica-rich crust may be metamorphized into felsic gneiss, rise, undergo partial melting and finally relaminate at the base of the crust. Consequently, it is plausible that most of the LCC lost into the mantle may have a more mafic composition compared to the rocks found at the base of the lithosphere.

The recycling of substantial masses of CC within the mantle can also have a significant impact on the mantle's composition. The recycled CC may represent a few percent of the mantle's mass, estimated at 1.6-2.3 wt%, and contribute to its enrichment in refractory elements. Research focusing on isotopic variations in ocean island basalts suggests that recycled CC may persist within the mantle and could be sampled through the hotspot-related volcanism. The predominant influence of recycled LCC has been proposed as an explanation for the characteristics of EM-I-like OIB (Boyet et al., 2019; Frey et al., 2002), thereby supporting the hypothesis of abundant LCC storing in the mantle.

5. Conclusions

We analyzed the Ce-Nd isotope compositions of Precambrian samples from Canada (composite in nature), Phanerozoic samples from western Europe, and Archean xenoliths from Siberia that represent the upper to lower parts of the continental crust. Both the Canadian upper crust and the West European deep crust closely align with the εCe-εNd mantle array whereas the deep crust of the Siberian craton plots to the left of the array. The peculiar composition of the deep crust in the Siberian craton can be explained by high grade-metamorphism related to large-scale delamination and rejuvenation of the Archean lower lithosphere at 1.8 Ga (Moyen et al., 2017). This process likely caused a preferential loss of La, resulting in decreased La/Ce ratios, while preserving the Archean Sm-Nd age systematics. This is consistent with the greater mobility of light REE relative to medium REE previously observed under granulite-facies conditions (Ague, 2017).

Comparing the measured parent/daughter ratios with a large set of granulites from the literature, we found that only Siberian xenoliths deviate significantly to the left of the εCe-εNd mantle array with time (high negative θ and high negative ΔεCe/Ga, representing the degree and rate of deviation, respectively). As a comparison, Archean and post-Archean literature granulites also have negative θ and ΔεCe/Ga but essentially to a lesser extent than the Siberian samples, making the latter exceptional cases in the LCC database. Most worldwide granulites exhibit a θ of -3° and can deviate from the εCe-εNd mantle array by ≈0.46 epsilon Ce units per billion years. Using this compilation, we propose new parent/daughter ratios for the LCC: $^{138}La/^{142}Ce = 0.00380$

±0.00007 and $^{147}Sm/^{144}Nd$ = 0.128 ±0.007. These findings suggest that high-grade metamorphism and/or reworking occurring in LCC conditions may lead to enhanced mobility of certain LREE in LCC rocks and deviation of the La-Ce and Sm-Nd isotopic systems from the mantle array over time.

The LCC represented by the granulite database cannot be reproduced by a typical mass-balance budget of the BSE. The later results in the isotope composition of the deep continental crust (MCC+LCC) far to the left of the εCe-εNd mantle array; it would require to incorporate a substantial proportion of Siberian-like granulites within the continents, although they are rare in the LCC database. Alternatively, incorporating a substantial proportion of LCC in mass-balance calculations, considering the massive recycling of LCC back into the mantle, provides a more reliable explanation. We estimate that approximately 3 to 5 times the mass of the continental crust has been recycled into the mantle throughout Earth's history, mostly comprising the LCC. This modeling brings the deep crust composition closer to the mantle array and aligns better with the constraints from the granulite database.

Acknowledgments

We thank D. Laporte for providing Beaunit, Bournac, and Ivrea samples, C. Fonquernie, C. Bosq, and D. Auclair for technical support, K.R. Ludwig for the use of his program IsoplotR, E. Hasenstab, A. Stracke and H. Downes as well as two anonymous reviewers for helpful comments that have improved the quality of this manuscript and the Geological Survey of Japan for providing the isotope reference

material JNdi-1. Reference material Ce_{LMV} is available upon request. This project received funding from the European Research Council (ERC) under the European Union's Horizon 2020 research and innovation program (Grant Agreements No. 682778 - ISOREE and No. 817934 - MILESTONE). A.V.G. was supported by the state assignment project of IGM SB RAS (No. 122041400157-9). This is Laboratory of Excellence ClerVolc contribution number XX.

Appendix A. Supplementary material

Supplementary material related to this article can be found online at XX.

Supplementary data 1: Major-, trace-element contents, and Ce-Nd isotopes.

Supplementary data 2: Database including Archean and post-Archean granulites from the literature.

Supplementary material: 1) Estimating the θ angle; 2) Parameters and equations used in mass-balance budget calculations.

References

Ague, J.J., 2017. Element mobility during regional metamorphism in crustal and subduction zone environments with a focus on the rare earth elements (REE). American Mineralogist 102, 1796–1821.

753 Allègre, C.J., Lewin, É., 1989. Chemical structure and history of the Earth: evidence
754 from global non-linear inversion of isotopic data in a three-box model. Earth and
755 Planetary Science Letters 96, 61–88.
756 Barrat, J.-A., Zanda, B., Moynier, F., Bollinger, C., Liorzou, C., Bayon, G., 2012.
757 Geochemistry of CI chondrites: Major and trace elements, and Cu and Zn isotopes.
758 Geochimica et Cosmochimica Acta 83, 79–92.
759 Bau, M., 1999. Scavenging of dissolved yttrium and rare earths by precipitating iron
760 oxyhydroxide: experimental evidence for Ce oxidation, Y-Ho fractionation, and
761 lanthanide tetrad effect. Geochimica et Cosmochimica Acta 63, 67–77.
762 Begemann, F., Ludwig, K.R., Lugmair, G.W., Min, K., Nyquist, L.E., Patchett, P.J.,
763 Renne, P.R., Shih, C.-Y., Villa, I.M., Walker, R.J., 2001. Call for an improved set
764 of decay constants for geochronological use. Geochimica et Cosmochimica Acta
765 65, 111–121.
766 Bellot, N., Boyet, M., Doucelance, R., Bonnand, P., Savov, I.P., Plank, T., Elliott, T.,
767 2018. Origin of negative cerium anomalies in subduction-related volcanic samples:
768 Constraints from Ce and Nd isotopes. Chemical Geology 500, 46–63.
769 Bellot, N., Boyet, M., Doucelance, R., Pin, C., Chauvel, C., Auclair, D., 2015. Ce
770 isotope systematics of island arc lavas from the Lesser Antilles. Geochimica et
771 Cosmochimica Acta 168, 261–279.
772 Berger, J., Féménias, O., Coussaert, N., Mercier, J.-C.C., Demaiffe, D., 2007.
773 Cumulating processes at the crust-mantle transition zone inferred from Permian
774 mafic-ultramafic xenoliths (Puy Beaunit, France). Contributions to Mineralogy and
775 Petrology 153, 557–575.
776 Bohlen, S.R., Mezger, K., 1989. Origin of Granulite Terranes and the Formation of the
777 Lowermost Continental Crust. Science 244, 326.

778 Bonnand, P., Israel, C., Boyet, M., Doucelance, R., Auclair, D., 2019. Radiogenic and
779 stable Ce isotope measurements by thermal ionisation mass spectrometry. Journal
780 of Analytical Atomic Spectrometry 34(3), 504–516.
781 Bouvier, A., Vervoort, J.D., Patchett, P.J., 2008. The Lu–Hf and Sm–Nd isotopic
782 composition of CHUR: Constraints from unequilibrated chondrites and
783 implications for the bulk composition of terrestrial planets. Earth and Planetary
784 Science Letters 273, 48–57.
785 Boyet, M., Doucelance, R., Israel, C., Bonnand, P., Auclair, D., Suchorski, K., Bosq,
786 C., 2019. New constraints on the origin of the EM-1 component revealed by the
787 measurement of the La-Ce isotope systematics in Gough Island lavas.
788 Geochemistry, Geophysics, Geosystems 20.
789 Chauvel, C., Garçon, M., Bureau, S., Besnault, A., Jahn, B., Ding, Z., 2014. Constraints
790 from loess on the Hf–Nd isotopic composition of the upper continental crust. Earth
791 and Planetary Science Letters 388, 48–58.
792 Dhuime, B., Hawkesworth, C.J., Delavault, H., Cawood, P.A., 2018. Rates of
793 generation and destruction of the continental crust: implications for continental
794 growth. Philosophical Transactions of the Royal Society A: Mathematical,
795 Physical and Engineering Sciences 376, 20170403.
796 Dickin, A.P., Jones, N.W., Thirlwall, M.F., Thompson, R.N., 1987. A Ce/Nd isotope
797 study of crustal contamination processes affecting Palaeocene magmas in Skye,
798 Northwest Scotland. Contributions to Mineralogy and Petrology 96, 455–464.
799 Downes, H., 1993. The nature of the lower continental crust of Europe: petrological
800 and geochemical evidence from xenoliths. Physics of the Earth and Planetary
801 Interiors 79, 195–218.

802 Downes, H., Dupuy, C., Leyreloup, A., 1990. Crustal evolution of the Hercynian belt
803 of Western Europe: Evidence from lower-crustal granulitic xenoliths (French
804 Massif Central). Chemical Geology 83, 209–231.
805 Féménias, O., Coussaert, N., Bingen, B., Whitehouse, M., Mercier, J.-C.C., Demaiffe,
806 D., 2003. A Permian underplating event in late-to post-orogenic tectonic setting.
807 Evidence from the mafic–ultramafic layered xenoliths from Beaunit (French
808 Massif Central). Chemical Geology 199, 293–315.
809 Féménias, O., Coussaert, N., Berger, J., Mercier, J.-C.C., Demaiffe, D., 2004.
810 Metasomatism and melting history of a Variscan lithospheric mantle domain:
811 evidence from the Puy Beaunit xenoliths (French Massif Central). Contrib Mineral
812 Petrol 148, 13–28.
813 Frey, F.A., Weis, D., Borisova, A.Y., Xu, G., 2002. Involvement of Continental Crust
814 in the Formation of the Cretaceous Kerguelen Plateau: New Perspectives from
815 ODP Leg 120 Sites, Journal of Petrology 43(7), 1207–1239.
816 Frossard, P., Israel, C., Bouvier, A., Boyet, M., 2022. Earth's composition was modified
817 by collisional erosion. Science 377, 1529–1532.
818 Gao, Y., Ling, W., Qiu, X., Chen, Z., Lu, S., Bai, Xiao, Bai, Xiujuan, Zhang, J., Yang,
819 H., Duan, R., 2016. Decoupled Ce-Nd isotopic systematics of the Neoproterozoic
820 Huangling intrusive complex and its geological significance, eastern Three Gorges,
821 South China. Journal of Earth Science 27, 864–873.
822 Gao, S., Luo, T.-C., Zhang, B.-R., Zhang, H.-F., Han, Y., Zhao, Z.-D., Hu, Y.-K., 1998.
823 Chemical composition of the continental crust as revealed by studies in East China.
824 Geochimica et Cosmochimica Acta 62, 1959–1975.

825 Garçon, M., Boyet, M., Carlson, R.W., Horan, M.F., Auclair, D., Mock, T.D., 2018.
826 Factors influencing the precision and accuracy of Nd isotope measurements by
827 thermal ionization mass spectrometry. Chemical Geology 476, 493–514.
828 Goldstein, S.J., Jacobsen, S.B., 1988. Nd and Sr isotopic systematics of river water
829 suspended material: implications for crustal evolution. Earth and Planetary Science
830 Letters 87, 249–265.
831 Hacker, B.R., Kelemen, P.B., Behn, M.D., 2015. Continental Lower Crust. Annual
832 Review of Earth and Planetary Sciences 43, 167–205.
833 Hacker, B.R., Kelemen, P.B., Behn, M.D., 2011. Differentiation of the continental crust
834 by relamination. Earth Planet Sci Lett 307, 501–516.
835 Handy, M.R., Franz, L., Heller, F., Janott, B., Zurbriggen, R., 1999. Multistage
836 accretion and exhumation of the continental crust (Ivrea crustal section, Italy and
837 Switzerland). Tectonics 18, 1154–1177.
838 Hasenstab-Dübeler, E., Münker, C., Tusch, J., Thiemens, M.M., Garbe-Schönberg, D.,
839 Strub, E., Sprung, P., 2023. Cerium-Nd isotope evidence for an incompatible
840 element depleted Moon. Earth and Planetary Science Letters 606, 118018.
841 Hasenstab, E., Tusch, J., Schnabel, C., Marien, C.S., Van Kranendonk, M.J., Smithies,
842 H., Howard, H., Maier, W.D., Münker, C., 2020. Evolution of the early to late
843 Archean mantle from Hf-Nd-Ce isotope systematics in basalts and komatiites from
844 the Pilbara Craton. Earth and Planetary Science Letters 116627.
845 Hayashi, T., Tanimizu, M., Tanaka, T., 2004. Origin of negative Ce anomalies in
846 Barberton sedimentary rocks, deduced from La–Ce and Sm–Nd isotope
847 systematics. Precambrian Research 135, 345–357.
848 Hofmann, A.W., Class, C., Goldstein, S.L., 2022. Size and Composition of the
849 MORB+OIB Mantle Reservoir. Geochemistry, Geophysics, Geosystems 23(8).

Hofmann, A.W., 1988. Chemical differentiation of the Earth: the relationship between mantle, continental crust, and oceanic crust. Earth and Planetary Science Letters 90, 297–314.

Ionov, D.A., Carlson, R.W., Doucet, L.S., Golovin, A.V., Oleinikov, O.B., 2015a. The age and history of the lithospheric mantle of the Siberian craton: Re–Os and PGE study of peridotite xenoliths from the Obnazhennaya kimberlite. Earth and Planetary Science Letters 428, 108–119.

Ionov, D.A., Doucet, L.S., Carlson, R.W., Golovin, A.V., Korsakov, A.V., 2015b. Post-Archean formation of the lithospheric mantle in the central Siberian craton: Re–Os and PGE study of peridotite xenoliths from the Udachnaya kimberlite. Geochimica et Cosmochimica Acta 165, 466–483.

Ionov, D.A., Doucet, L.S., Ashchepkov, I.V., 2010. Composition of the lithospheric mantle in the Siberian craton: new constraints from fresh peridotites in the Udachnaya-East kimberlite. Journal of Petrology 51, 2177–2210.

Israel, C., Boyet, M., Doucelance, R., Bonnand, P., Frossard, P., Auclair, D., Bouvier, A., 2020. Formation of the Ce-Nd mantle array: Crustal extraction vs. recycling by subduction. Earth and Planetary Science Letters 530, 115941.

Jochum, K.P., Weis, U., Schwager, B., Stoll, B., Wilson, S.A., Haug, G.H., Andreae, M.O., Enzweiler, J., 2016. Reference values following ISO guidelines for frequently requested rock reference materials. Geostandards and Geoanalytical Research 40, 333–350.

Jackson, M.G., Jellinek, A.M., 2013. Major and trace element composition of the high 3He/4He mantle: Implications for the composition of a nonchonditic Earth. Geochemistry, Geophysics, Geosystems 14, 2954–2976.

874 Johnston, S., Brandon, A., McLeod, C., Rankenburg, K., Becker, H., Copeland, P.,
875 2022. Nd isotope variation between the Earth–Moon system and enstatite
876 chondrites. Nature 611, 501–506.
877 Kamenetsky, V.S., Kamenetsky, M.B., Golovin, A.V., Sharygin, V.V., Maas, R., 2012.
878 Ultrafresh salty kimberlite of the Udachnaya–East pipe (Yakutia, Russia): A
879 petrological oddity or fortuitous discovery? Lithos 152, 173–186.
880 Kinny, P., Griffin, B., Heaman, L., Brakhfogel, F., Spetsius, Z., 1997. SHRIMP U-Pb
881 ages of perovskite from Yakutian kimberlites. Geologiya i geofizika 38, 91–99.
882 Koreshkova, M., Downes, H., 2021. The age of the lower crust of the central part of the
883 Columbia supercontinent: A review of zircon data. Gondwana Research 96, 37–
884 55.
885 Koreshkova, M.Yu., Downes, H., Levsky, L.K., Vladykin, N.V., 2011. Petrology and
886 geochemistry of granulite xenoliths from Udachnaya and Komsomolskaya
887 kimberlite pipes, Siberia. Journal of Petrology 52, 1857–1885.
888 Kumari, S., Paul, D., Stracke, A., 2016. Open system models of isotopic evolution in
889 Earth's silicate reservoirs: implications for crustal growth and mantle
890 heterogeneity. Geochimica and Cosmochimica Acta 195, 142–157.
891 Langone, A., Zanetti, A., Daczko, N.R., Piazolo, S., Tiepolo, M., Mazzucchelli, M.,
892 2018. Zircon U-Pb dating of a lower crustal shear zone: a case study from the
893 northern sector of the Ivrea-Verbano Zone (Val Cannobina, Italy). Tectonics 37,
894 322–342.
895 Lee, S.-G., Asahara, Y., Tanaka, T., Kim, N.H., Kim, K.H., Yi, K., Masuda, A., Song,
896 Y.S., 2010. La–Ce and Sm–Nd isotopic systematics of early Proterozoic
897 leucogranite with tetrad REE pattern. Chemical Geology 276, 360–373.

898 Lee, S.-G., Masuda, A., Shimizu, H., Song, Y.-S., 2001. Crustal evolution history of
899 Korean Peninsula in East Asia: The significance of Nd, Ce isotopic and REE data
900 from the Korean Precambrian gneisses. Geochemical Journal 35, 175–187.
901 Liu, C.-Q., Shimizu, H., Nakai, S., Xie, G.-H., Masuda, A., 1990. Isotopic and trace
902 element studies for Cenozoic volcanic rocks from western China: implication for a
903 crust-like enriched component in the mantle. Geochemical Journal 24, 327–342.
904 Lodders, K., Fegley, B., 1998. The planetary scientist's companion. Oxford University
905 Press on Demand.
906 Maas, R., Kamenetsky, M.B., Sobolev, A.V., Kamenetsky, V.S., Sobolev, N.V., 2005.
907 Sr, Nd, and Pb isotope evidence for a mantle origin of alkali chlorides and
908 carbonates in the Udachnaya kimberlite, Siberia. Geol 33, 549.
909 Makishima, A., Masuda, A., 1994. Ce isotope ratios of N-type MORB. Chemical
910 Geology 118, 1–8.
911 McCulloch, M.T., Wasserburg, G.J., 1978. Sm-Nd and Rb-Sr Chronology of
912 Continental Crust Formation: Times of addition to continents of chemically
913 fractionated mantle-derived materials are determined. Science 200, 1003–1011.
914 McDonough, W.F., Sun, S.-S., 1995. The composition of the Earth. Chemical Geology
915 120, 223–253.
916 McLennan, S.M., 2001. Relationships between the trace element composition of
917 sedimentary rocks and upper continental crust. Geochemistry, Geophysics,
918 Geosystems, 2(4).
919 Meija, J., Coplen, T.B., Berglund, M., Brand, W.A., De Bièvre, P., Gröning, M.,
920 Holden, N.E., Irrgeher, J., Loss, R.D., Walczyk, T., Prohaska, T., 2016. Isotopic
921 compositions of the elements 2013 (IUPAC Technical Report). Pure and Applied
922 Chemistry 88(3), 293–306.

923 Minami, M., Shimizu, H., Masuda, A., Adachi, M., 1995. Two Archean Sm-Nd ages
924 of 3.2 and 2.5 Ga for the Marble Bar Chert, Warrawoona Group, Pilbara Block,
925 Western Australia. Geochemical Journal 29, 347–362.
926 Moreira, H., Dhuime, B., Ionov, D., Buzenchi, A., Gusev, N., 2023. Hafnium isotope
927 systematics of zircon in high-grade metamorphic rocks of the Anabar shield,
928 Siberia: Radiogenic Hf without mantle input? Chemical Geology 636, 121644.
929 Moyen, J.-F., Paquette, J.-L., Ionov, D., Gannoun, A., Korsakov, A., Golovin, A.,
930 Moine, B., 2017. Paleoproterozoic rejuvenation and replacement of Archaean
931 lithosphere: Evidence from zircon U–Pb dating and Hf isotopes in crustal xenoliths
932 at Udachnaya, Siberian craton. Earth and Planetary Science Letters 457, 149–159.
933 Peressini, G., Quick, J.E., Sinigoi, S., Hofmann, A.W., Fanning, M., 2007. Duration of
934 a Large Mafic Intrusion and Heat Transfer in the Lower Crust: a SHRIMP U-Pb
935 Zircon Study in the Ivrea-Verbano Zone (Western Alps, Italy). Journal of Petrology
936 48, 1185–1218.
937 Poupinet, G., Shapiro, N.M., 2009. Worldwide distribution of ages of the continental
938 lithosphere derived from a global seismic tomographic model. Lithos 109, 125–
939 130.
940 Quick, J.E., Sinigoi, S., Mayer, A., 1994. Emplacement dynamics of a large mafic
941 intrusion in the lower crust, Ivrea-Verbano Zone, northern Italy. Journal of
942 Geophysical Research 99, 21559–21573.
943 Quick, J.E., Sinigoi, S., Snoke, A.W., Kalakay, T.J., Mayer, A., Peressini, G., 2003.
944 Geologic map of the southern Ivrea-Verbano Zone, northwestern Italy. USGS,
945 Geological Investigation Series Map I-2776.
946 Reimink, J.R., Davies, J.H.F.L., Moyen, J.F., Pearson, D.G., 2023. A whole-lithosphere
947 view of continental growth. Geochemical Perspectives Letters 26, 45–49.

948 Rosas, J.C., Korenaga, J., 2018. Rapid crustal growth and efficient crustal recycling in
949 the early Earth: Implications for Hadean and Archean geodynamics. Earth and
950 Planetary Science Letters 494, 42–49.
951 Rossi, P., Cocherie, A., Fanning, C.M., Deloule, É., 2006. Variscan to eo-Alpine events
952 recorded in European lower-crust zircons sampled from the French Massif Central
953 and Corsica, France. Lithos 87, 235–260.
954 Rudnick, R.L., 1992. Xenoliths samples of the lower continental crust. Continental
955 lower crust, Elsevier, Amsterdam 23, 269–316.
956 Rudnick, R.L., Gao, S., 2014. Composition of the continental crust, in: Holland, H.D.,
957 Turekian, K.K. (Eds.), Treatise on Geochemistry. Pergamon, Oxford, 1–51.
958 Sato, J., Hirose, T., 1981. Half-life of ^{138}La. Radiochemical and Radioanalytical Letters
959 46, 145–152.
960 Schuster, R., Stüwe, K., 2008. Permian metamorphic event in the Alps. Geol 36, 603.
961 Shatsky, V.S., Malkovets, V.G., Belousova, E.A., Tretiakova, I.G., Griffin, W.L.,
962 Ragozin, A.L., Wang, Q., Gibsher, A.A., O'Reilly, S.Y., 2018. Multi-stage
963 modification of Paleoarchean crust beneath the Anabar tectonic province (Siberian
964 craton). Precambrian Research 305, 125–144.
965 Shatsky, V.S., Wang, Q., Skuzovatov, S.Yu., Ragozin, A.L., 2019. The crust-mantle
966 evolution of the Anabar tectonic province in the Siberian Craton: Coupled or
967 decoupled? Precambrian Research 332, 105388.
968 Shaw, D.M., Dostal, J., Keays, R.R., 1976. Additional estimates of continental surface
969 Precambrian shield composition in Canada. Geochimica et Cosmochimica Acta 40,
970 73–83.

971 Shaw, D.M., Reilly, G.A., Muysson, J.R., Pattenden, G.E., Campbell, F.E., 1967. An
972 estimate of the chemical composition of the Canadian Precambrian Shield.
973 Canadian Journal of Earth Sciences 4, 829–853.
974 Shimizu, H., Amakawa, H., Sawatari, H., Masuda, A., 1990. Estimation of light rare
975 earth element patterns in original sources for rocks from their Ce and Nd isotopic
976 ratios. Journal of the Mass Spectrometry Society of Japan 38, 107–113.
977 Shimizu, H., Lee, S.-G., Masuda, A., Adachi, M., 1996. Geochemistry of Nd and Ce
978 isotopes and REE abundances in Precambrian orthogneiss clasts from the Kamiaso
979 conglomerate, central Japan. Geochemical Journal 30, 57–69.
980 Shimizu, H., Nakai, S., Tasaki, S., Masuda, A., Bridgwater, D., Nutman, A.,
981 Baadsgaard, H., 1988. Geochemistry of Ce and Nd isotopes and REE abundances
982 in the Amitsoq gneisses, West Greenland. Earth and Planetary Science Letters 91,
983 159–169.
984 Shimizu, H., Tanaka, T., Masuda, A., 1984. Meteoritic $^{138}Ce/^{142}Ce$ ratio and its
985 evolution. Nature 307, 251–252.
986 Stracke, A., Bizimis, M., Salters, V.J., 2003. Recycling oceanic crust: Quantitative
987 constraints. Geochemistry, Geophysics, Geosystems 4(3).
988 Tanaka, T., Shimizu, H., Kawata, Y., Masuda, A., 1987. Combined La–Ce and Sm–Nd
989 isotope systematics in petrogenetic studies. Nature 327, 113–117.
990 Tang, M., Rudnick, R.L., McDonough, W.F., Gaschnig, R.M., Huang, Y., 2015.
991 Europium anomalies constrain the mass of recycled lower continental crust.
992 Geology 43, 703–706.
993 Tanimizu, M., 2000. Geophysical determination of the ^{138}La β−decay constant.
994 Physical Review. C 62, 017601.

995 Tanimizu, M., Tanaka, T., 2002. Ce-Nd-Sr isotope systematics of eucrites and lunar
996 rocks, in: origin of elements in the Solar System. Springer, 555–572.
997 Taylor, S.R., McLennan, S.M., 1995. The geochemical evolution of the continental
998 crust. Reviews of Geophysics 33, 241.
999 Taylor, S.R., McLennan, S., 1981. The composition and evolution of the continental
1000 crust: rare earth element evidence from sedimentary rocks. Philosophical
1001 Transactions of the Royal Society of London. Series A, Mathematical and Physical
1002 Sciences 301, 381–399.
1003 Tazoe, H., Obata, H., Gamo, T., 2007. Determination of cerium isotope ratios in
1004 geochemical samples using oxidative extraction technique with chelating resin.
1005 Journal of Analytical Atomic Spectrometry 22, 616.
1006 Tusch, J., Hoffmann, J.E., Hasenstab, E., Fischer-Gödde, M., Marien, C.S., Wilson,
1007 A.H., Münker, C., 2022. Long-term preservation of Hadean protocrust in Earth's
1008 mantle. Proceedings of the National Academy of Sciences 119, e2120241119.
1009 Vermeesch, P., 2018. IsoplotR: A free and open toolbox for geochronology. Geoscience
1010 Frontiers 9, 1479–1493.
1011 Vervoort, J.D., Patchett, P.J., Albarède, F., Blichert-Toft, J., Rudnick, R., Downes, H.,
1012 2000. Hf–Nd isotopic evolution of the lower crust. Earth and Planetary Science
1013 Letters 181, 115–129.
1014 Voshage, H., Hofmann, A., Mazzucchelli, M., Rivalenti, G., Sinigoi, S., Raczek, I.,
1015 Demarchi, G., 1990. Isotopic evidence from the Ivrea Zone for a hybrid lower crust
1016 formed by magmatic underplating. Nature 347, 731.
1017 Weaver, B.L., Tarney, J., 1984. Empirical approach to estimating the composition of
1018 the continental crust. Nature 310, 575–577.

White, W.M., Klein, E.M., 2014. Composition of the Oceanic Crust, in: Treatise on Geochemistry. Elsevier, 457–496.

Willig, M., Stracke, A., 2019. Earth's chondritic light rare earth element composition: Evidence from the Ce–Nd isotope systematics of chondrites and oceanic basalts. Earth and Planetary Science Letters 509, 55–65.

Willig, M., Stracke, A., Beier, C., Salters, V.J.M., 2020. Constraints on mantle evolution from Ce-Nd-Hf isotope systematics. Geochimica et Cosmochimica Acta 272, 36–53.

Table caption:

Table 1. La-Ce and Sm-Nd isotope measurements. Uncertainties reported on Ce and Nd measured isotope ratios are 2se analytical errors in the last decimal place. Cerium and Nd isotopic compositions are expressed in present-day $\varepsilon Ce = \left(\frac{\frac{^{138}Ce}{^{142}Ce}_{sample}}{\frac{^{138}Ce}{^{142}Ce}_{CHUR}} - 1 \right) \times 10{,}000$ and $\varepsilon Nd = \left(\frac{\frac{^{143}Nd}{^{144}Nd}_{sample}}{\frac{^{143}Nd}{^{144}Nd}_{CHUR}} - 1 \right) \times 10{,}000$ using the following CHUR references: $^{138}Ce/^{142}Ce = 0.02256577$ (Israel et al., 2020) and $^{143}Nd/^{144}Nd = 0.512630$ (Bouvier et al., 2008). εCe_t and εNd_t are isotopic compositions corrected from radioactive decay using published ages for the West European samples, 3.0 Ga for the Canadian samples (see section 2.1) and the 2.7 Ga Sm-Nd errorchron age for the Siberian rocks (Fig. 4). Parent/daughter ratios were obtained using the natural isotope abundances of Meija et al. (2016): $^{138}La/^{142}Ce = La/Ce \times 0.00804772$; $^{147}Sm/^{144}Nd = Sm/Nd \times 0.60455923$. CHUR values for parent/daughter ratios are $^{138}La/^{142}Ce = 0.00311$ and $^{147}Sm/^{144}Nd = 0.1960$ (Bouvier et al., 2008 ; Israel et al., 2020). Decay

constant values are $\lambda_{\beta,\ 138La} = 2.37 \times 10^{-12}$ yr^{-1}, $\lambda_{EC,\ 138La} = 4.44 \times 10^{-12}$ yr^{-1} (Sato and Hirose, 1981; Shimizu et al., 1984; Tanimizu, 2000) and $\lambda_{147Sm} = 6.539 \times 10^{-12}$ yr^{-1} (Begemann et al., 2001).

Table 2. Elemental and isotopic compositions of Earth's main silicate reservoirs. BSE, bulk silicate Earth; EDR, early depleted reservoir; DMM, depleted MORB mantle; CC, continental crust; UCC, upper continental crust; MCC, middle continental crust; LCC, lower continental crust. Isotopic compositions for CC and MCC+LCC reservoirs are estimated using mass-balance calculations for a chondritic BSE and an EDR. Errors given for the mass-balance calculated isotopic compositions (CC, MCC+LCC) and the mass fraction of the continental crust (m_{bulkCC}/m_{BSE}) correspond to the standard deviation on the mean value calculated for the composition models of Rudnick and Gao (2014) and Hacker et al. (2015 – mafic and felsic model). Errors on literature data are 2 sd. Values in italics refer to literature data: [a*] based on Lu content from McDonough and Sun, 1995 and chondritic REE ratios from Israel et al., 2020 and Bouvier et al., 2008; [b] from Israel et al., 2020; [c] from Bouvier et al., 2008; [d] from Rudnick and Gao, 2014; [e] and [f] correspond to felsic and mafic compositions from Hacker et al., 2015, [g] from Allègre and Lewin, 1989; Chauvel et al., 2014; Goldstein and Jacobsen, 1988. [d*], [e*], and [f*] are recalculated after modification of the relative proportions of CC sub-reservoirs. [h*]Cerium and Nd concentrations and εCe-εNd values of the EDR are estimated using the method suggested in Jackson and Jellinek, 2013 for a Sm/Nd ratio increased by 2.65%

Figure captions

Fig. 1. Total alkali *versus* silica (TAS) diagram for West European, Canadian and Siberian samples from this study (colored large circles and diamonds) and literature (white squares – Koreshkova et al., 2011; Moyen et al., 2017; Shatsky et al., 2019, 2018). Literature granulites are from Hacker et al., 2015 with an additional 670 new data points from the literature (grey squares are Archean granulites and pink squares are post-Archean granulites – see Supplementary data 2 for references). Stars represent reference composition for LCC, MCC and UCC from Rudnick and Gao, 2014 (R&G) and Hacker et al., 2015 (most mafic and felsic models – $H+_{mafic}$ and $H+_{felsic}$). We chose not to represent any subdivision in the TAS diagram to compare the silica and alkali contents in all our metaigneous and metasedimentary samples with literature data, without consideration of their rock type. IV9 is out of limits of this diagram (SiO_2 content is 32 wt.% and Na_2O+K_2O content is 3.3 wt.%)

Fig. 2. Bulk-CC normalized REE patterns for samples from this study together with values for UCC, MCC and LCC from Rudnick and Gao (2014). The Siberian samples are divided into two distinct graphs according to their Sm/Nd ratio (samples with Sm/Nd >0.24 and <0.24 are in graphs b and d respectively), and their felsic or mafic composition. Three Udachnaya kimberlites from Maas et al., 2005 are also represented.

Fig. 3. εNd *versus* εCe measured in the Siberian, Canadian, and West European samples. CC samples from literature are reported for comparison (Gao et al., 2016; Hasenstab et al., 2020; Hayashi et al., 2004; Israel et al., 2020; Lee et al., 2010, 2001; Liu et al., 1990; Minami et al., 1995; Shimizu et al., 1996, 1990, 1988, 1988; Tanaka et al., 1987; Tazoe et al., 2007; Tusch et al., 2022). The black line is the mantle array regression line (Israel et al., 2020 – $\varepsilon Nd = -7.3\ (\pm 0.5) \times \varepsilon Ce + 0.4\ (\pm 0.3)$), the dark grey

1092 area shows the mean dispersion of OIB on both sides of the mantle array (±0.2 εCe and
1093 ±1.3εNd) and light grey area shows their maximum dispersion (±0.9εCe and ±6.3εNd).
1094
1095 **Fig. 4**. (a) La-Ce and (b) Sm-Nd errorchron diagrams for the Siberian samples and for
1096 granulite xenoliths from Udachnaya (Koreshkova et al., 2011). Regression lines and
1097 errorchron ages (±2 sd) are calculated using model 3 of IsoplotR with 1% errors on
1098 Sm/Nd ratios and 0.3% errors on La/Ce ratios. None of the regressions define an
1099 isochron (MSWD values of 11 and 28 for (a) and (b), respectively). Two Udachnaya
1100 kimberlites from Maas et al., 2005 are also represented.
1101
1102 **Fig. 5.** $\varepsilon Nd_{(0\rightarrow t)}$ *versus* $\varepsilon Ce_{(0\rightarrow t)}$ diagram representing Ce-Nd isotopic paths (arrows)
1103 calculated from measured La/Ce and Sm/Nd ratios and present-day Ce-Nd isotopic
1104 compositions. (a) Correction for radioactive decay was done using published ages of
1105 0.257, 0.200, and 0.270 Ga for the samples from Beaunit, Bournac, and Ivrea,
1106 respectively, and 3.0 Ga for the Canadian samples (see section 2.1). (b) Correction for
1107 radioactive decay was done using the 2.7 Ga Sm-Nd errorchron age for the Siberian
1108 rocks. The Ce-Nd mantle array regression line is from Israel et al. (2020). (c)
1109 Representation of hypothetical isotopic paths (arrows) related to their oriented angle θ,
1110 with the mantle array (thick grey line), estimated in degrees in an orthonormal system.
1111 The θ value depends only on the La/Ce and Sm/Nd ratios. Evolution trends pointing
1112 toward the left of the mantle array have negative θ values, or positive θ values if they
1113 point to the right of the mantle array. The zero (or 180°) value means the evolution
1114 trend of the sample is parallel to the mantle array. $f_{Sm/Nd}$ and $f_{La/Ce}$ describe the evolution
1115 of a sample relative to the chondritic reference, where $f_{Sm/Nd}$ =
1116 $(({}^{147}Sm/{}^{144}Nd_{sample}/{}^{147}Sm/{}^{144}Nd_{CHUR})-1)$ and $f_{La/Ce}$ =

1117 (($^{138}La/^{142}Ce_{sample}/^{138}La/^{142}Ce_{CHUR}$)-1). Sample 386-13 is presented as an example. Its
1118 isotopic path shows an angle with the mantle array equal to -9.8°. Note that angles
1119 observed in a classical εCe-εNd space are distorted due to the large difference of scale
1120 between the x and y axes of the diagram (see miniature for angles represented in an
1121 orthonormal diagram).
1122
1123 **Fig. 6.** Geographical distribution of literature samples used for their La, Ce, Nd and Sm
1124 contents, presented in pie charts (a) for Archean samples and (b) for post-Archean
1125 samples.
1126
1127 **Fig. 7.** (a) ΔεCe per billion years *versus* θ and (b) $^{138}La/^{142}Ce$ *versus* $^{147}Sm/^{144}Nd$
1128 diagrams estimated for the European, Canadian and Siberian samples from this study
1129 and compared to Archean (n = 445) and post-Archean granulites (n = 1136) from
1130 literature. Histograms are also associated with both variables of the diagram for
1131 Archean and post-Archean granulites, and Siberian crustal xenoliths (data from this
1132 study and Koreshkova et al., 2011 and Shatsky et al., 2019) together with their Kernel
1133 Density Estimation (KDE – calculated using IsoplotR – grey, pink and red curves,
1134 respectively). ΔεCe is calculated as the relative horizontal deviation from the mantle
1135 array after one billion years of evolution, using initial isotopic compositions located on
1136 the mantle array and measured parent/daughter ratios. The dark grey and light grey
1137 fields in (a) represent the mean and maximum horizontal scatter of OIBs that are used
1138 to define the εCe-εNd mantle array, respectively. The dotted line represents the linear
1139 regression calculated from Archean and post-Archean samples using IsoplotR for θ
1140 values between -5 and -1° (n = 411). Its equation is ΔεCe/Ga = 0.15 (±0.03) × θ -0.01
1141 (±0.05). Reference parent/daughter values for the LCC from Rudnick and Gao, 2014

(R&G) and Hacker et al., 2015 (mafic and felsic models – $H+_{mafic}$ and $H+_{felsic}$, respectively) are represented in (b) as black, blue and green lines and stars, respectively. Parent/daughter ratios resulting in isotopic compositions evolving along the mantle array ($\theta = 0°$) and with an angle of -3° relative to the mantle array are represented as black and purple lines, respectively.

Scale for θ is limited between -20 and 20° to improve readability (bin size 1° – 249 samples out of scale, including IV1 with $\theta = -176°$). Scales are also limited between 0.001 and 0.010 for $^{138}La/^{142}Ce$ (bin size 0.0002 – 17 samples out of scale) and between 0.025 and 0.25 for $^{147}Sm/^{144}Nd$ (bin size 0.005 – 53 samples out of scale) to improve readability.

Fig. 8. εCe *versus* εNd measured in mantle-derived samples (Bellot et al., 2018, 2015; Dickin et al., 1987; Israel et al., 2020; Makishima and Masuda, 1994; Tanaka et al., 1987; Willig and Stracke, 2019; Willig et al., 2020) and in crustal samples (references in Fig. 3). The orange and grey fields represent mass-balance calculated isotopic compositions for the bulk CC and for the MCC+LCC, respectively, for both chondritic and non-chondritic compositions of the BSE, using parameters in Table 2 and relative proportions of the CC sub-reservoirs from Rudnick and Gao, 2014. The red and black fields represent mass-balance calculated isotopic compositions for the bulk CC and for the MCC+LCC, respectively, using parameters in Table 2 for a bulk CC after modifying the relative proportions of UCC, MCC and LCC (8.1, 7.6 and 84.3%, respectively – thick lines for Rudnick and Gao based compositions). The purple lines represent the equidistant lines from the mantle array for $\Delta\varepsilon Ce = -0.8$ and -1.1, estimated for 1.8 and 2.4 Ga-old granulites, using $\Delta\varepsilon Ce/Ga = -0.46$.

Sample	$^{138}La/^{142}Ce$	$^{138}Ce/^{142}Ce$	2se	εCe	$εCe_t$	$^{147}Sm/^{144}Nd$	$^{143}Nd/^{144}Nd$	2se	εNd	$εNd_t$
Bournac – Crustal xenoliths										
BOU2	0.00428	0.02256804	37	1.01	0.8	0.155	0.512308	5	-6.28	-5.2
BOU3	0.00374	0.02257441	24	3.83	3.7	0.118	0.512240	6	-7.61	-5.6
BOU4	0.00385	0.02256812	21	1.04	0.9	0.121	0.512251	6	-7.39	-5.5
Ivrea – Verbano zone - Uplifted crust										
IV1	0.00254	0.02256429	22	-0.65	-0.5	0.219	0.512975	4	6.73	5.9
IV5a	0.00407	0.02256904	24	1.45	1.2	0.121	0.512183	4	-8.72	-6.1
IV5b	0.00486	0.02256883	22	1.36	0.9	0.115	0.512113	4	-10.09	-7.3
IV9	0.00410	0.02256910	14	1.47	1.2	0.140	0.511876	3	-14.72	-12.8
IV10	0.00401	0.02256961	19	1.70	1.4	0.107	0.512391	4	-4.66	-1.6
Puy Beaunit – Crustal xenoliths										
B4-Glite	0.00387	0.02256509	22	-0.30	-0.5	0.147	0.512778	5	2.89	4.5
B6	0.00477	0.02256668	20	0.40	-0.0	0.096	0.512572	6	-1.12	2.2
B152	0.00388	0.02256895	24	1.41	1.2	0.109	0.512101	5	-10.31	-7.5
BG4	0.00434	0.02256718	22	0.62	0.3	0.117	0.512556	4	-1.44	1.1
BPG1	0.00372	0.02256718	17	0.63	0.5	0.149	0.512391	5	-4.67	-3.1
BPG2	0.00368	0.02256490	22	-0.39	-0.5	0.156	0.512718	3	1.72	3.0
BG6	0.00483	0.02256894	23	1.41	0.9	0.122	0.512216	6	-8.08	-5.6
B2-gneiss	0.00448	0.02256892	23	1.39	1.0	0.081	0.512020	4	-11.90	-8.1
Udachnaya pipe, Siberian craton – Crustal xenoliths										
1001-16	0.00363	0.02257045	25	2.07	0.6	0.094	0.510823	1	-35.25	0.1
1003-14	0.00283	0.02256514	23	-0.28	0.5	0.150	0.512000	1	-12.30	3.8
1006-14	0.00187	0.02256183	19	-1.75	1.8	0.140	0.511519	2	-21.48	-2.6
1006-16	0.00329	0.02256663	27	0.38	-0.1	0.115	0.511147	1	-28.93	-0.8
1010-13	0.00314	0.02256687	20	0.49	0.4	0.150	0.511923	2	-13.80	2.0
1014-14	0.00461	0.02257248	20	2.97	-1.3	0.099	0.511155	2	-28.78	5.1
226-03	0.00357	0.02256808	19	1.03	-0.3	0.149	0.511979	2	-12.70	3.8
231-17	0.00325	0.02256714	22	0.61	0.2	0.118	0.511197	2	-27.95	-0.7
232-17	0.00336	0.02256859	26	1.25	0.5	0.155	0.511932	1	-13.62	0.7
246-17	0.00242	0.02256238	21	-1.50	0.5	0.172	0.512390	1	-4.69	3.7
322-13	0.00362	0.02256835	22	1.14	-0.3	0.113	0.511202	1	-27.86	0.9
360-13	0.00373	0.02257041	20	2.05	0.3	0.121	0.511220	2	-27.51	-1.3
370-13	0.00600	0.02257880	19	5.78	-2.5	0.069	0.510497	2	-41.61	2.6
386-13	0.00284	0.02256410	23	-0.74	0.0	0.132	0.511520	1	-21.66	0.5
98-13	0.00270	0.02256459	27	-0.52	0.6	0.111	0.511188	2	-28.14	1.6
Precambrian shield, Canadian craton – Crustal composite										
NQ	0.00392	0.02257114	32	2.38	-0.2	0.109	0.511368	2	-24.38	9.2
BI	0.00387	0.02257188	31	2.71	0.3	0.105	0.511033	1	-30.91	4.2
SS	0.00423	0.02257179	38	2.67	-0.9	0.100	0.511044	2	-30.69	6.4
SQ	0.00311	0.02256581	30	0.02	0.0	0.113	0.512300	1	-6.19	25.4

Table 1

Chondritic	**Earth**								
		DMM	**UCC**	**CC**	**MCC**	**LCC**	**CC**	**MCC**	**LCC**
	BSE	**(mean MORB)**	**(mean loess)**				**84% LCC**		
% of CC				*100*	*29.6* [d]	*38.8* [c]	100	7.6	84.3
Ce (µg/g)	1.7 [a*]		*63* [d]	*43* [d] | *49* [e] |*36* [f]	*53* [d] | *39* [e] |*27* [f]	*20* [d] | *46* [e] |*19* [f]	26 [d*] | 47 [e*] |23 [f*]		
Nd (µg/g)	1.3 [a*]		*27* [d]	*20* [d] | *23* [e] |*19* [f]	*25* [d] | *19* [e] |*16* [f]	*11* [d] | *22* [e] |*13* [f]	13 [d*] | 22 [e*] |14 [f*]		
εCe	*0.00 ±0.29* [b]	*-1.1 ±0.6* [b]	*1.8 ±0.3* [b]	1.1 ±0.3 to 0.2 ±0.2	0.4 ±0.3 to -1.1 ±0.5		1.3 ±0.7 to 0.4 ±0.4	1.2 ±0.8 to 0.1 ±0.4	
εNd	*0.00 ±0.21* [c]	*9.7 ±2.3* [b]	*-11.2 ±3.0* [b]	*-21 to -10* [g]	-28.1 ±2.4 to -9.2 ±0.2		*-21 to -10* [g]	-22.6 ± 0.8 to -9.8 ±0.1	
m_{bulkCC}/m_{BSE}				*0.026 ±0.013*			*0.033 ±0.022*		
Early	**Depleted**	**Earth**							
	EDR	**DMM**	**UCC**	**CC**	**MCC**	**LCC**	**CC**	**MCC**	**LCC**
		(mean MORB)	**(mean loess)**				**84% LCC**		
% of CC				*100*	*29.6* [d]	*38.8* [c]	100	7.6	84.3
Ce (µg/g)	1.5 [h*]		*63* [d]	*43* [d] | *49* [e] |*36* [f]	*53* [d] | *39* [e] |*27* [f]	*20* [d] | *46* [e] |*19* [f]	26 [d*] | 47 [e*] |23 [f*]		
Nd (µg/g)	1.2 [h*]		*27* [d]	*20* [d] | *23* [e] |*19* [f]	*25* [d] | *19* [e] |*16* [f]	*11* [d] | *22* [e] |*13* [f]	13 [d*] | 22 [e*] |14 [f*]		
εCe	-0.3 [h*]	*-1.1 ±0.6* [b]	*1.8 ±0.3* [b]	1.2 ±0.3 to 0.4 ±0.2	0.7 ±0.42 to -0.9 ±0.4		1.5 ±0.7 to 0.5 ±0.5	1.4 ±0.9 to 0.3 ±0.4	
εNd	3.1 [h*]	*9.7 ±2.3* [b]	*-11.2 ±3.0* [b]	*-21 to -10* [g]	-28.1 ±2.4 to -9.2 ±0.2		*-21 to -10* [g]	-22.6 ±0.8 to -9.8 ±0.1	
m_{bulkCC}/m_{EDR}				*0.016 ±0.008*			*0.024 ±0.011*		

Table 2

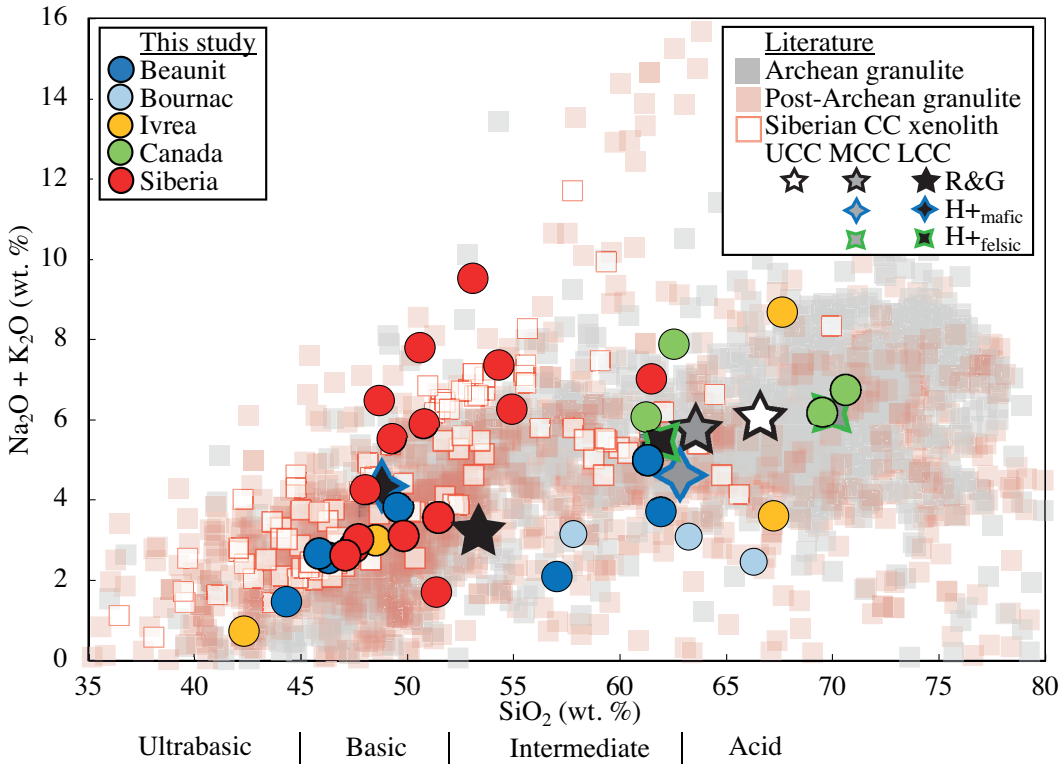
This study
Beaunit
Bournac
Ivrea
Canada
Siberia
Literature
Archean granulite
Post-Archean granulite
Siberian CC xenolith
UCC MCC LCC
R&G
H+mafic
H+felsic
Na2O + K2O (wt. %)
SiO2 (wt. %)
Ultrabasic
Basic
Intermediate
Acid

Figure 1

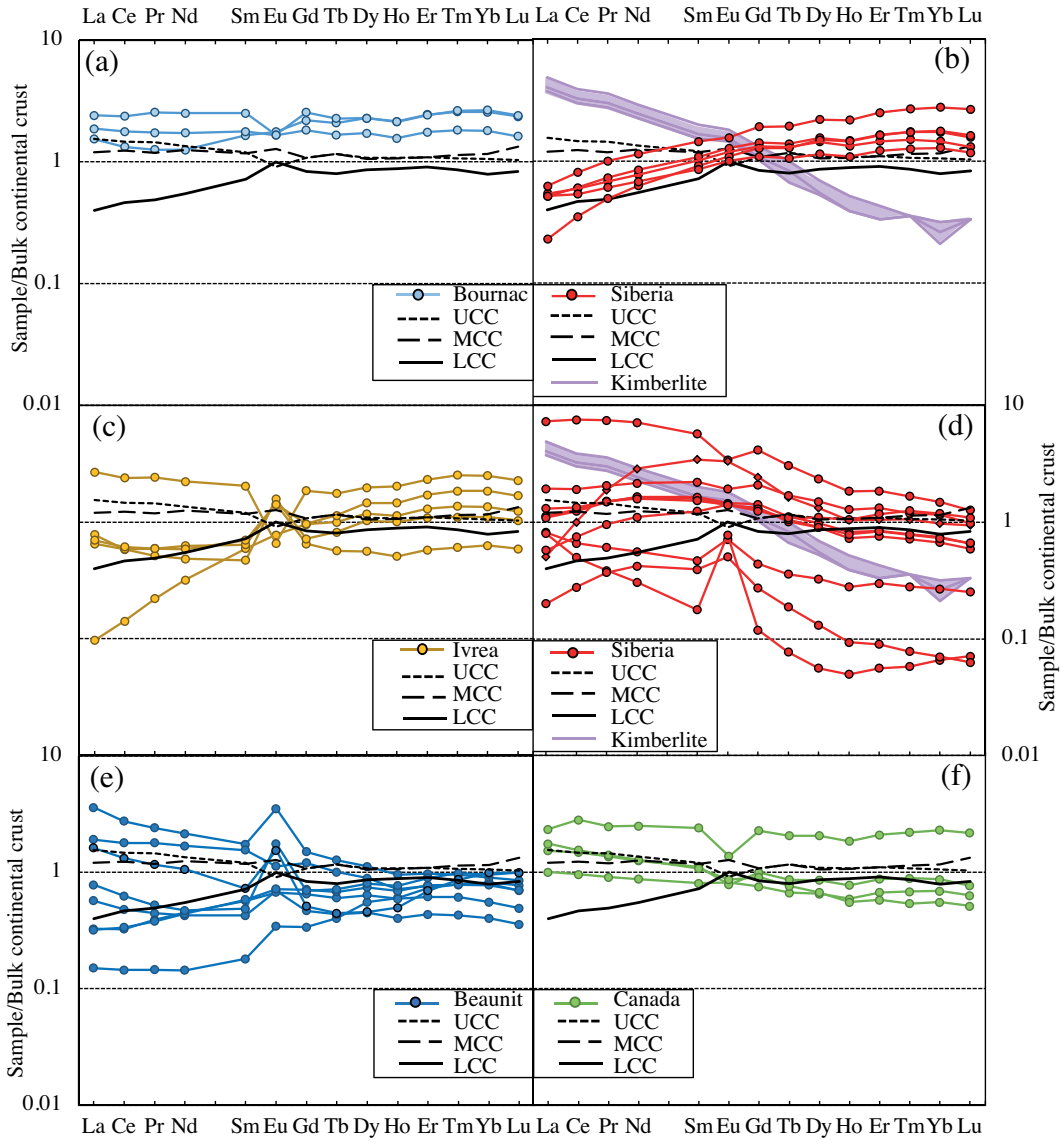
La Ce Pr Nd Sm Eu Gd Tb Dy Ho Er Tm Yb Lu
(a)
(b)
(c)
(d)
(e)
(f)
Sample/Bulk continental crust
10
1
0.1
0.01
Bournac
UCC
MCC
LCC
Siberia
Kimberlite
Ivrea
Beaunit
Canada

Figure 2

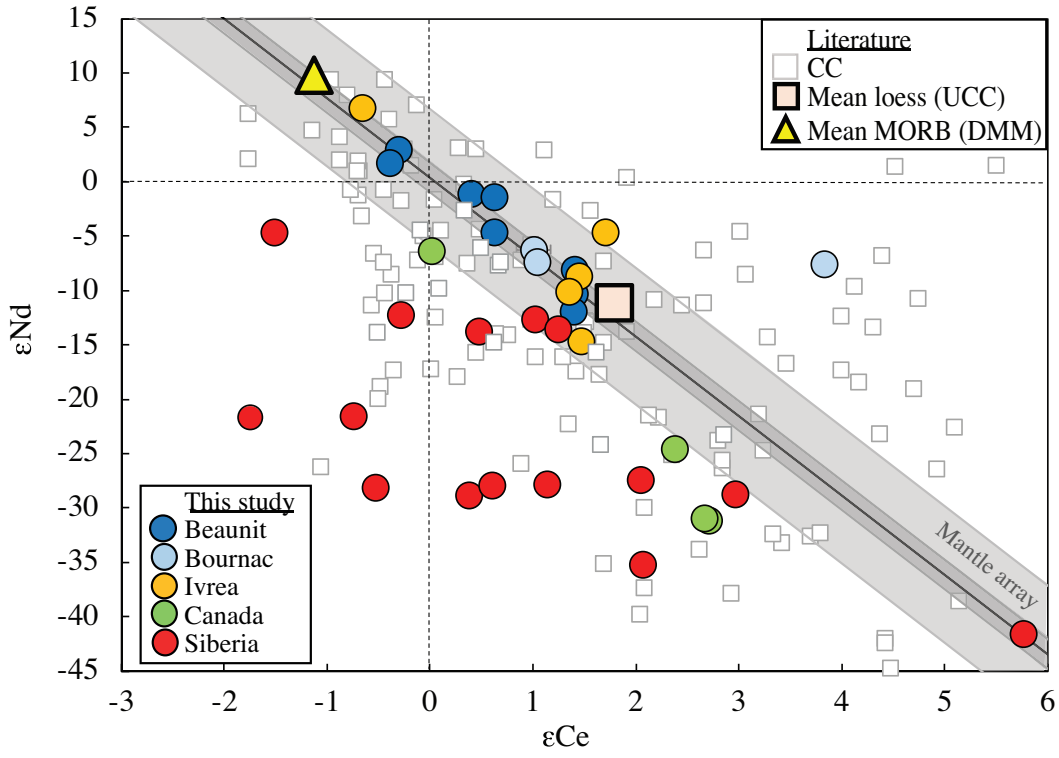
Literature
CC
Mean loess (UCC)
Mean MORB (DMM)
This study
Beaunit
Bournac
Ivrea
Canada
Siberia
Mantle array
εNd
εCe
15
10
5
0
-5
-10
-15
-20
-25
-30
-35
-40
-45
-3
-2
-1
0
1
2
3
4
5
6

Figure 3

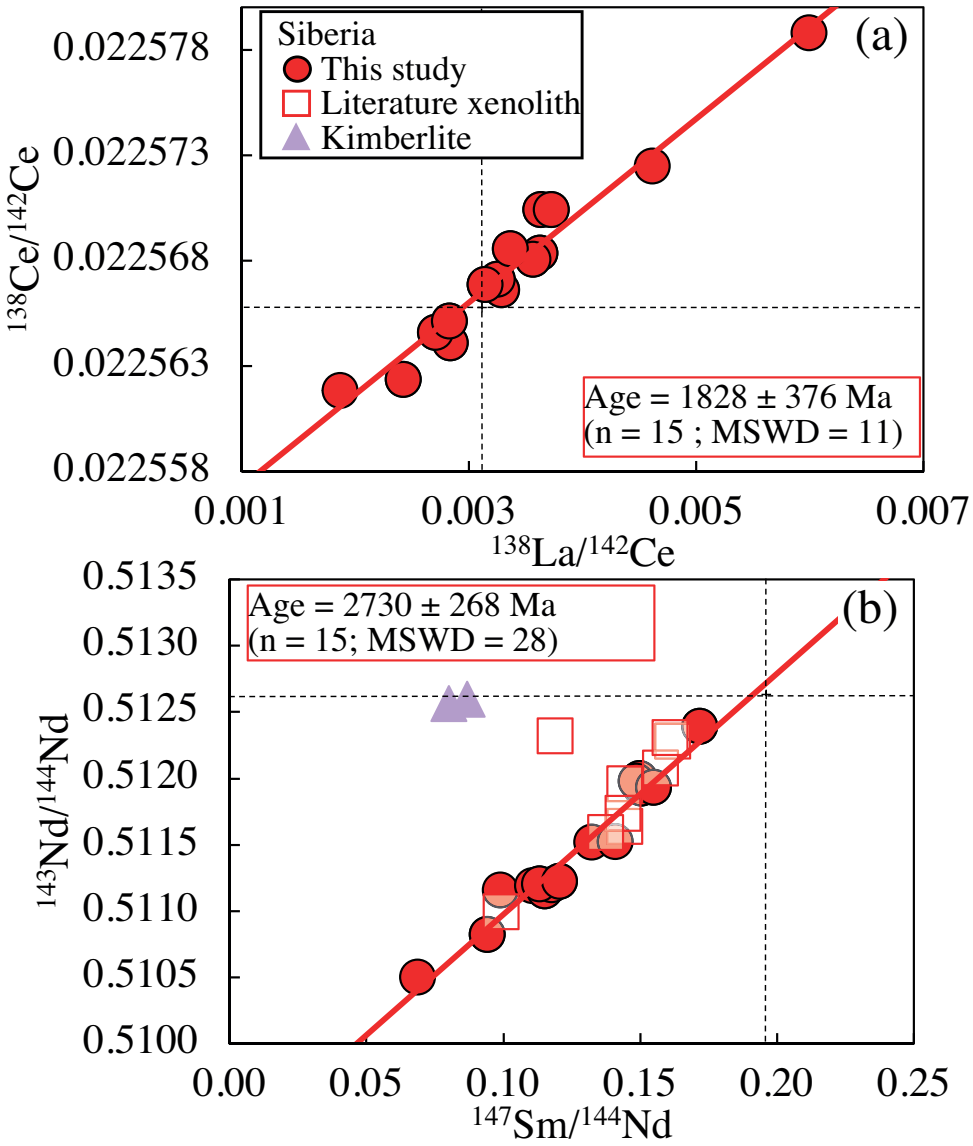
Siberia
This study
Literature xenolith
Kimberlite
(a)
Age = 1828 ± 376 Ma
(n = 15 ; MSWD = 11)
0.022578
0.022573
0.022568
0.022563
0.022558
$^{138}Ce/^{142}Ce$
0.001
0.003
0.005
0.007
$^{138}La/^{142}Ce$
(b)
Age = 2730 ± 268 Ma
(n = 15; MSWD = 28)
0.5135
0.5130
0.5125
0.5120
0.5115
0.5110
0.5105
0.5100
$^{143}Nd/^{144}Nd$
0.00
0.05
0.10
0.15
0.20
0.25
$^{147}Sm/^{144}Nd$

Figure 4

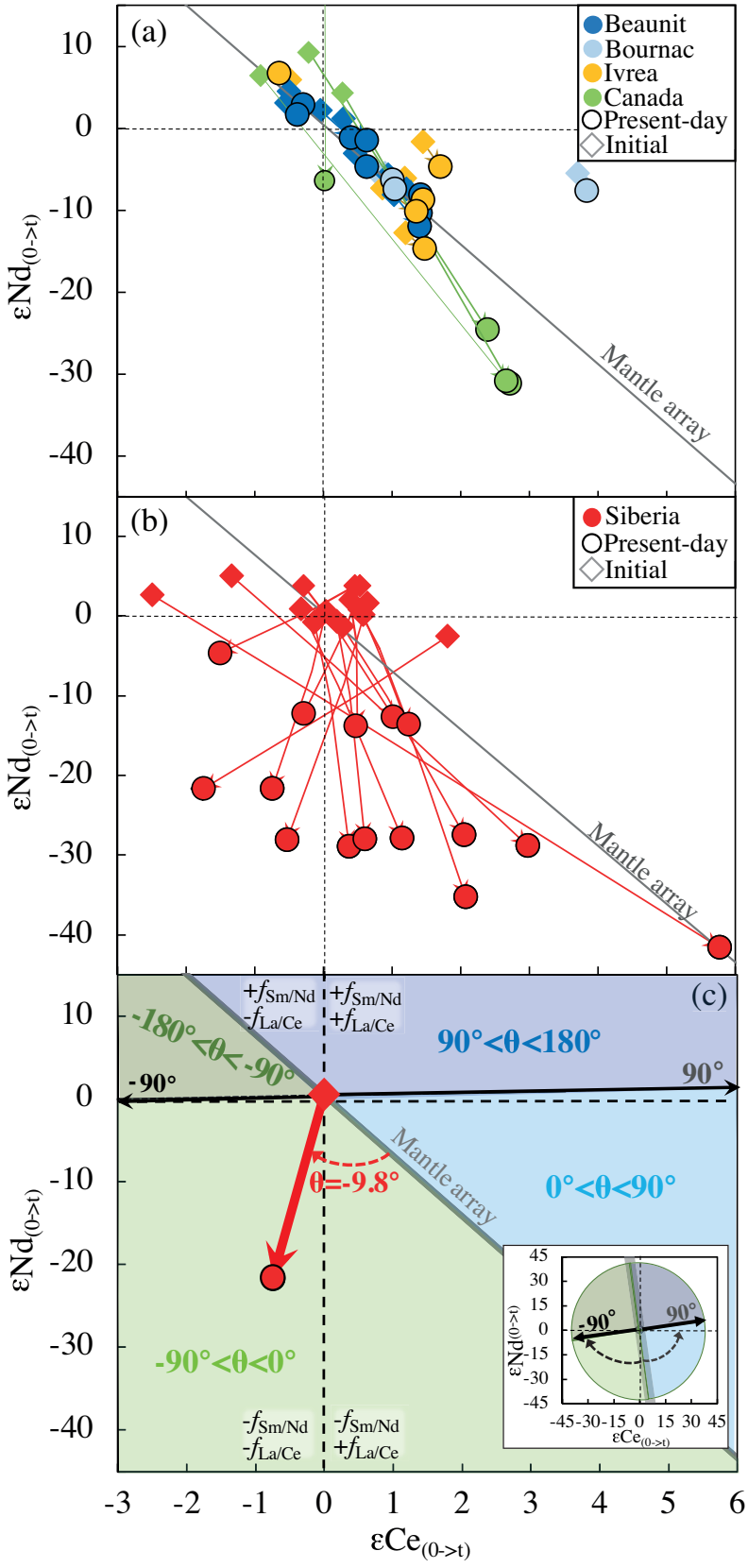
(a)
Beaunit
Bournac
Ivrea
Canada
Present-day
Initial
Mantle array
(b)
Siberia
Present-day
Initial
Mantle array
(c)
+fSm/Nd -fLa/Ce
+fSm/Nd +fLa/Ce
-180°<θ<-90°
90°<θ<180°
-90°
90°
θ=-9.8°
Mantle array
0°<θ<90°
-90°<θ<0°
-fSm/Nd -fLa/Ce
-fSm/Nd +fLa/Ce
εNd(0->t)
εCe(0->t)

Figure 5

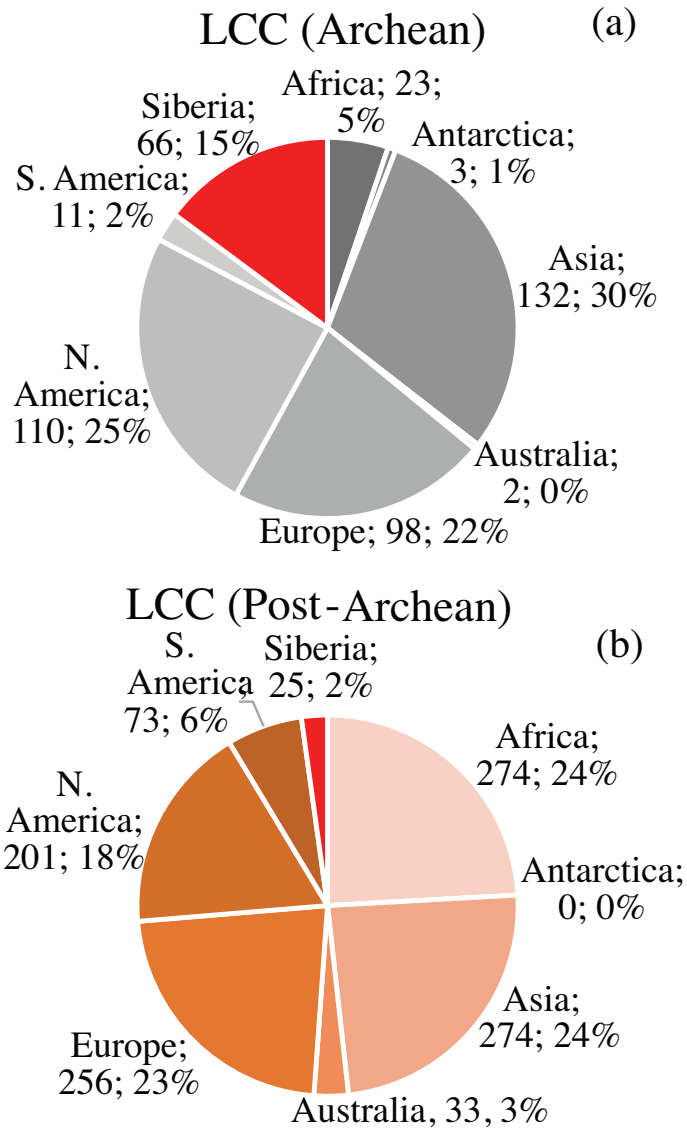
LCC (Archean)
(a)
Africa; 23; 5%
Antarctica; 3; 1%
Asia; 132; 30%
Australia; 2; 0%
Europe; 98; 22%
N. America; 110; 25%
S. America; 11; 2%
Siberia; 66; 15%
LCC (Post-Archean)
(b)
Africa; 274; 24%
Antarctica; 0; 0%
Asia; 274; 24%
Australia, 33, 3%
Europe; 256; 23%
N. America; 201; 18%
S. America 73; 6%
Siberia; 25; 2%

Figure 6

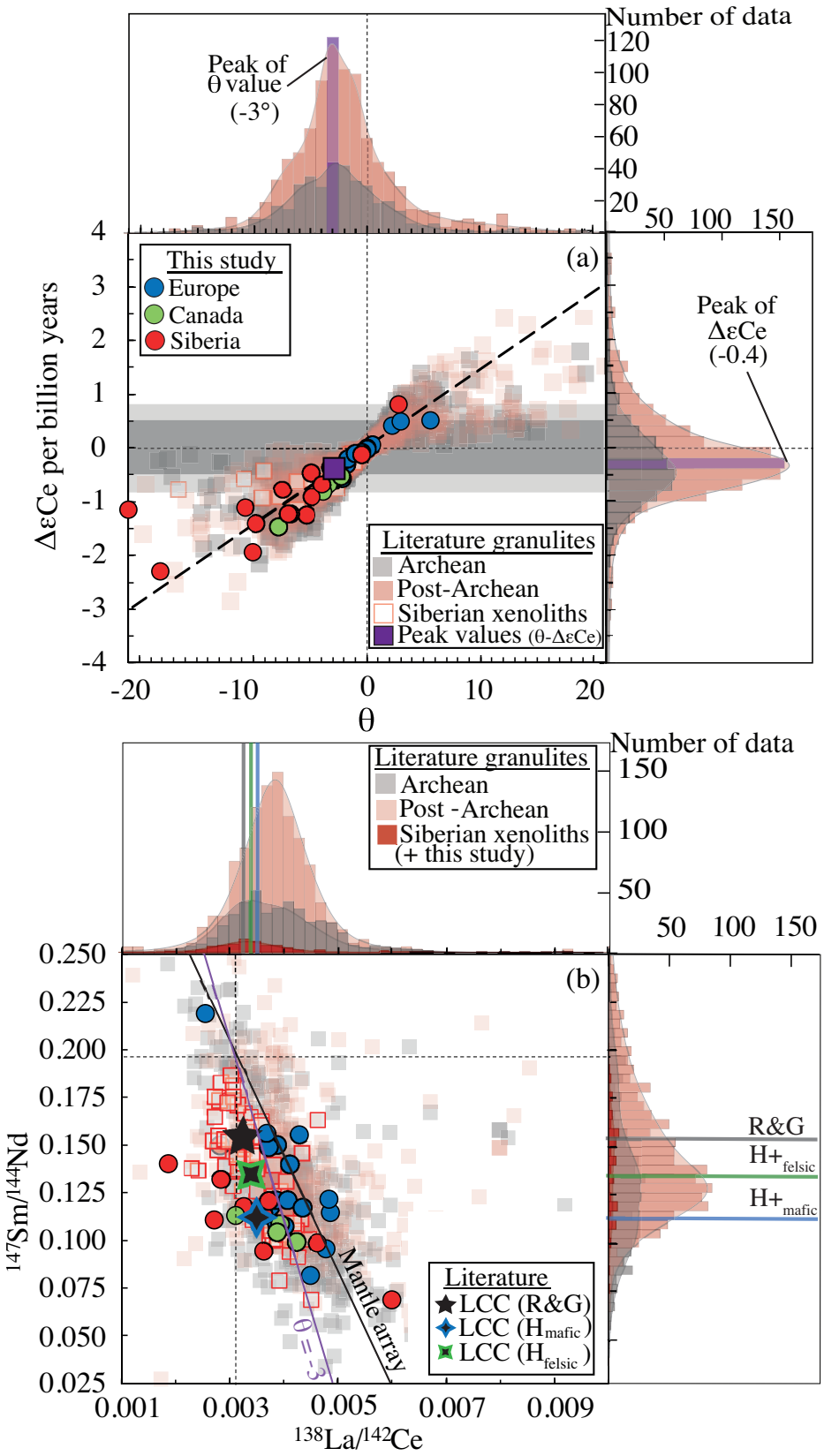
Number of data
Peak of
θ value
(-3°)
This study
Europe
Canada
Siberia
(a)
Peak of
ΔεCe
(-0.4)
ΔεCe per billion years
Literature granulites
Archean
Post-Archean
Siberian xenoliths
Peak values (θ-ΔεCe)
θ
Literature granulites
Archean
Post -Archean
Siberian xenoliths
(+ this study)
(b)
R&G
H+felsic
H+mafic
Literature
LCC (R&G)
LCC (Hmafic)
LCC (Hfelsic)
Mantle array
θ=-3
147Sm/144Nd
138La/142Ce

Figure 7

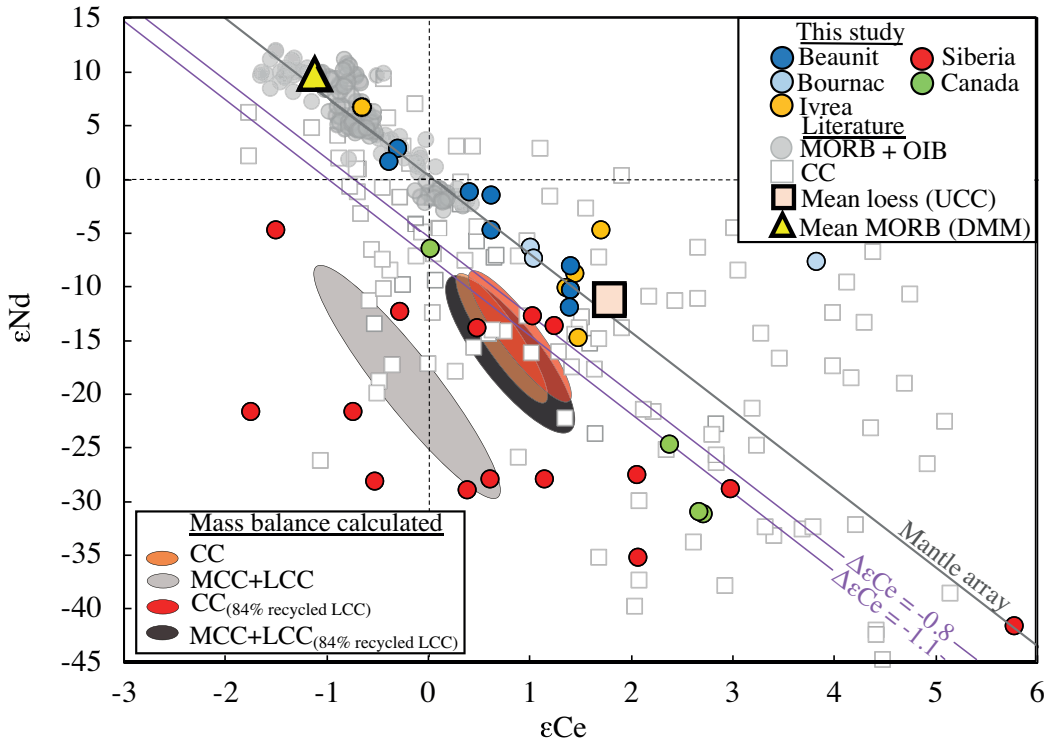
This study
Beaunit
Siberia
Bournac
Canada
Ivrea
Literature
MORB + OIB
CC
Mean loess (UCC)
Mean MORB (DMM)
Mass balance calculated
CC
MCC+LCC
CC(84% recycled LCC)
MCC+LCC(84% recycled LCC)
Mantle array
ΔεCe = -0.8
ΔεCe = -1.1
εNd
εCe
15
10
5
0
-5
-10
-15
-20
-25
-30
-35
-40
-45
-3
-2
-1
0
1
2
3
4
5
6

Figure 8

SUPPLEMENTARY MATERIAL

FIRST CE-ND ISOTOPE MEASUREMENTS OF MIDDLE AND LOWER CONTINENTAL CRUST SAMPLES SUPPORT MASSIVE LOWER CRUST RECYCLING OVER EARTH'S HISTORY

C. ISRAEL[1,2,*], M. BOYET[1], R. DOUCELANCE[1], P. BONNAND[1,3], B. DHUIME[4], D. IONOV[4], H. MOREIRA[4], M.G. JACKSON[5], A.V. GOLOVIN[6]

[1] Université Clermont Auvergne, CNRS, IRD, OPGC, Laboratoire Magmas et Volcans, F-63000 Clermont-Ferrand, France

[2] Institut de Physique du Globe de Paris, 75005 Paris, France

[3] Univ Brest, CNRS, Laboratoire Geo-Ocean, UMR6538, IUEM, 29280, Plouzane, France

[4] Univ Montpellier & CNRS, Géosciences Montpellier, France

[5] Department of Earth Science, University of California, Santa Barbara, CA, 93106-9630, USA

[6] Sobolev Institute of Geology and Mineralogy, Siberian Branch, Russian Academy of Science, Novosibirsk 630090, Russia

*Corresponding author.

E-mail address: israel@ipgp.fr (Claudine Israel).

1. Estimating the θ angle

The $\theta_{\text{sample-mantle array}}$ angle is the angle existing between the evolution vector of any sample and the vector representing the mantle array, in a εCe-εNd diagram (epsilon values calculated at zero for the present-day value of the sample and at any time t by using the CHUR value at the same time t). The equation of the mantle array is $\varepsilon Nd = \varepsilon Ce \times -7.3 + 0.4$ (Israel et al., 2020)

We first fix the initial isotopic composition of any sample on the mantle array. In this case, we chose εCe_i=0 and εNd_i=0.4 as the intercept of the mantle array. We use the CHUR value for cerium when calculating εCe.

We estimate the isotopic composition of a sample as the result of radioactive decay over a period t (here fixed at 1 Ga), using the measured parent/daughter ratios (εCe_t and εNd_t).

The horizontal distance $\Delta\varepsilon Ce_{sample-\text{MA}}$ between a sample and the mantle array is solely due to the radioactive decay, and is expresses as:

$$\Delta\varepsilon Ce_{sample-\text{MA}} = \varepsilon Ce_t - \frac{\varepsilon Nd_t - 0.4}{-7.3}$$

The norm of the evolution vector of a sample in an orthonormal diagram is:

$$N_{Ve,\text{sample}} = \sqrt{(\varepsilon Ce_t - \varepsilon Ce_i)^2 + (\varepsilon Nd_t - \varepsilon Nd_i)^2}$$

Similarly, we estimate the norm of the mantle array as a vector, by considering $\varepsilon Ce_A - \varepsilon Ce_B = 1$ and $\varepsilon Nd_A - \varepsilon Nd_B = -7.3$ because for a variation of εCe of +1 between a point A and a point B, the variation of εNd is -7.3, according to the equation of the mantle array in a plot of εNd vs εCe :

$$N_{Ve,MA} = \sqrt{(\varepsilon Ce_A - \varepsilon Ce_B)^2 + (\varepsilon Nd_A - \varepsilon Nd_B)^2} = \sqrt{1^2 + (-7.3)^2}$$

We then estimate the vector product of these vectors:

$$P_{Ve} = (\varepsilon Ce_A - \varepsilon Ce_B) \times (\varepsilon Ce_t - \varepsilon Ce_i) + (\varepsilon Nd_A - \varepsilon Nd_B) \times (\varepsilon Nd_t - \varepsilon Nd_i)$$

The cosine of the angle between these two vectors is:

$$\text{Cos}(\theta) = \frac{P_{Ve}}{\sqrt{N_{Ve,sample} \times N_{Ve,MA}}}$$

And finally the angle is Arc(Cos(θ)).

However, the calculated angle is not oriented. We set θ to be negative if $\Delta\varepsilon Ce_{sample-\text{MA}}$ is negative (the isotopic composition of the sample tends to evolve below the mantle array). Or θ is positive if $\Delta\varepsilon Ce_{sample-\text{MA}}$ is positive (the isotopic composition of the sample tends to evolve above the mantle array).

2. Parameters and equations used in mass-balance budget calculations

Table S1: Elemental and isotopic compositions of Earth's silicate reservoirs used in mass-balance calculations: BSE, bulk silicate Earth; DMM, depleted MORB mantle (DMM = mean MORB); CC, continental crust; UCC, upper continental crust; MCC, middle continental crust; LCC, lower continental crust. Values in italics refer to literature data: Ce, Nd contents and Ce/Nd ratios are from Rudnick and Gao (R&G) and Hacker et al., 2015 (H et al. - for both mafic and felsic model) for CC, UCC and MCC+LCC reservoirs and they are calculated from Lu contents from McDonough and Sun, 1995 and chondritic REE ratios (see Israel et al., 2020 for further details). εCe and εNd values for DMM (mean MORB) and UCC (mean loess) are from Israel et al., 2020. εNd values for the bulk CC correspond to the entire range of suggested compositions for this reservoir in the literature (εNd = -21 to -10 according to Allègre and Lewin, 1989 and Chauvel et al., 2014, respectively). Note that the LCC accounts for 56.7 wt% of the MCC+LCC reservoir.

	Reservoir	Ce (µg/g)	Nd (µg/g)	Ce/Nd	εCe	εNd	W
	BSE	*1.7*	*1.3*	*1.28*	*0.00*	*0.00*	
	DMM				*-1.1*	*9.7*	
R&G	Bulk CC	*43*	*20*	*2.15*	1.0 – 0.2	*-21 – -10*	0.020 – 0.032
	UCC	*63*	*27*	*2.33*	*1.8*	*-11.2*	
	MCC+LCC	*34*	*17*	*2.01*	-1.1 – 0.3	-28 – -9	
H et al.,	Bulk CC	*36*	*19*	*1.89*	1.3 – 0.4	-21 – -10	0.022 – 0.034
Most mafic model	MCC+LCC	*22*	*14*	*1.57*	0.6 – -1.3	-29 – -9	
H et al.,	Bulk CC	*49*	*23*	*2.13*	1.0 – 0.2	-21 – -10	0.018 – 0.028
Most felsic model	MCC+LCC	*43*	*21*	*2.08*	0.5 – -0.8	-27 – -9	

Our single-stage differentiation model considers the continental crust (CC) and the depleted MORB mantle (DMM) to be complementary reservoirs developed from the primitive mantle (BSE).

The Nd sialic index (W_{Nd}) is defined as the amount of Nd in the continental crust relative to the total amount of Nd in the BSE (Allègre and Lewin, 1989). Its value can be obtained from the $^{143}Nd/^{144}Nd$ ratios of the BSE, DMM, and CC as:

$$\frac{143Nd}{144Nd_{BSE}} = W_{Nd} \times \frac{143Nd}{144Nd_{CC}} + (1 - W_{Nd}) \times \frac{143Nd}{144Nd_{DMM}}. \quad (1)$$

The Nd sialic index can also be approximated as the product of the mass fraction of continental crust (W, relative to the BSE) and the ratio of the Nd contents in the continental crust and BSE as:

$$W_{Nd} = W \times \frac{[\mathrm{Nd}]_{CC}}{[\mathrm{Nd}]_{BSE}} \quad \text{where } W = \frac{m_{cc}}{m_{CC}+m_{DMM}}. \quad (2)$$

Using W as obtained above, the Ce sialic index (W_{Ce}) and the Ce isotopic composition of the continental crust can be deduced from equations similar to equations (1) and (2):

$$W_{Ce} = W \times \frac{[\mathrm{Ce}]_{CC}}{[\mathrm{Ce}]_{BSE}}, \quad (4)$$

$$\frac{138Ce}{142Ce_{BSE}} = W_{Ce} \times \frac{138Ce}{142Ce_{CC}} + (1 - W_{Ce}) \times \frac{138Ce}{142Ce_{DMM}}. \quad (3)$$

The mass fraction of continental crust W also allows us to recalculate the complementary Nd and Ce contents of the DMM using mass-balance equations for the trace element concentrations:

$$[\mathrm{Nd}]_{BSE} = W \times [\mathrm{Nd}]_{CC} + (1 - W) \times [\mathrm{Nd}]_{DMM}, \quad (5)$$

$$[\mathrm{Ce}]_{BSE} = W \times [\mathrm{Ce}]_{CC} + (1 - W) \times [\mathrm{Ce}]_{DMM}. \quad (6)$$

To maintain a consistent dataset between isotopic and elemental ratios, the Ce and Nd concentrations of the DMM are recalculated using the BSE and CC contents and the mass fraction of DMM determined in step 2, where the mass fraction of DMM = 1 – mass fraction of CC.

The mass fraction of mantle depleted by the extraction of the continental crust is then:

$$\frac{m_{DM}}{m_{PM}} = \frac{m_{CC}}{m_{PM}} \times \frac{1-W}{W} \quad (7)$$

Where the typical present-day mass of the continental crust (m_{cc}) is 2.367×10^{25}g and the mass of the primitive mantle (m_{PM}) is 4.007×10^{27}g (Lodders and Fegley, 1998).

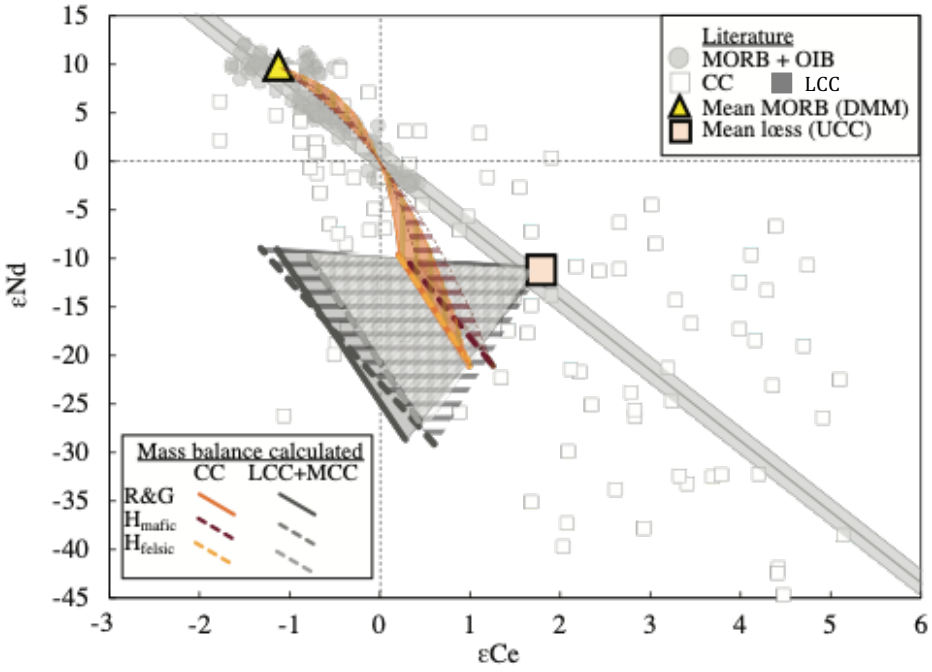

Figure S1: (a) εCe vs. εNd diagram representing the calculated crustal reservoirs by mass-balance calculation. Epsilon values are normalized according to the CHUR references defined for Nd with $^{143}Nd/^{144}Nd_{CHUR} = 0.512630$, $^{147}Sm/^{144}Nd = 0.196$. The orange, stripped dark red and stripped light orange fields represent the different hyperbolic DMM–CC mixing curves calculated for a chondritic BSE with Nd and Ce contents from Rudnick and Gao and Hacker et al., 2015 for extremely mafic and felsic CC models, respectively. Similarly, the grey, striped dark grey and striped light grey fields represent the UCC–(MCC-LCC) mixing lines using Nd and Ce contents from Rudnick and Gao, 2003 and Hacker et al., 2015. Note that the information given by the parent/daughter ratios of the UCC, MCC and LCC requires the MCC and LCC to have a higher Nd isotopic composition ($Sm/Nd_{LCC}>Sm/Nd_{MCC}>Sm/Nd_{UCC}$) and lower Ce isotopic composition ($La/Ce_{LCC}<La/Ce_{MCC}<La/Ce_{UCC}$) than the UCC. Our calculations are based on the entire range of literature estimates for the Nd isotopic composition of the bulk CC.